Progress in Energy and Combustion Science 49 (2015) 40–58

Contents lists available at ScienceDirect

Progress in Energy and Combustion Science

journal homepage: www.elsevier.com/locate/pecs

Review

Fundamental models for flow batteries

Q. Xu, T.S. Zhao*

Department of Mechanical and Aerospace Engineering, The Hong Kong University of Science and Technology, Clear Water Bay, Kowloon, Hong Kong Special Administrative Region

ARTICLE INFO

Article history:
Received 10 September 2014
Accepted 9 February 2015
Available online 13 March 2015

Keywords:
Flow batteries
Numerical modeling
Battery performance prediction

ABSTRACT

The flow battery is a promising technology for large-scale storage of intermittent power generated from solar and wind farms owing to its unique advantages such as location independence, scalability and versatility. The widespread commercialization of flow batteries, thus far, is still hindered by certain technical barriers. Removal of these barriers requires a fundamental understanding of the complex electrochemical and transport behaviors of flow batteries. Mathematical modeling and simulation serve important roles in the exploration of these complex phenomena and to the prediction as well as improvement of the cell performance of different system designs. In this review, a comprehensive study is performed to review and summarize state-of-the-art flow batteries and to provide an outlook on the future and potential of flow battery modeling. The review begins with a description of the physical and chemical processes of common flow batteries, followed by the detailed discussion of the governing equations for transports of mass, momentum, heat and charge as well as the electrochemical reactions for porous-medium models. The determination of key transport properties for the porous-medium models and their effects on modeling results are also analyzed. In addition, lattice Boltzmann method, molecular dynamics and density function simulations as well as stack-level network models for flow batteries are reviewed. Finally, the issues facing the future of flow battery modeling are addressed.

Contents

* Corresponding author. Tel.: +852 2358 8647; fax: +852 2358 1543.
E-mail address: metzhao@ust.hk (T.S. Zhao).

http://dx.doi.org/10.1016/j.pecs.2015.02.001
0360-1285/

1. Introduction

An increase in the utilization of carbon-free, renewable energy sources is the ultimate solution in reducing the impact of CO_2 emissions associated with the use of carbon-based energy sources on the climate. Some major renewable energy sources, including wind and solar energy, can supply a significant amount of electrical energy worldwide. However, the intermittent and fluctuant nature of these renewable sources substantially limit their reliability, and are major reasons why currently only comprise a small percentage of primary energy sources [1]. The potential of renewables can only be fully exploited if efficient, safe, and reliable electrical energy storage systems are developed. Over the past few decades, a number of different energy storage technologies have emerged. However, many of them possess inherent limitations and disadvantages, categorizing them to be economically and practically fit for only a narrow range of applications. Among different energy storage technologies, electrochemical systems are superior to others [2,3], primarily because they can provide direct conversion between chemical energy and electrical energy, and offer unique advantages, including low environmental footprints (can be sited near residential areas) and short response time (millisecond timescale, such that they can be used simultaneously for both power quality and energy management applications) [4,5].

In comparison to different electrochemical energy storage technologies such as capacitors or supercapacitors, lead-acid batteries, Ni-metal batteries, and Li-ion batteries, redox flow batteries are the most suitable for large-scale stationary energy storage [6–9]. They offer unique features, including but not limited to: i) low maintenance, ii) tolerance to deep discharge without risk of damage, iii) long lifetime (generally thousands of charge–discharge cycles) compared to that of galvanic batteries and, iv) simplicity in building large systems based on module design [10–17]. In addition, unlike other battery systems, energy is stored in the electrolyte solutions and the capacity of the system is determined by the concentration of the active redox couple species and the electrolyte tank volume of the redox flow battery, while the power rating of the system is determined by the number of cells in the stack and the electrode area. As such, the power and energy capacity of an RFB system can be designed separately.

The rapidly approaching commercialization of redox flow batteries sets a series of new challenges in developing the technology: notably, scale-up and optimization (with respect to electrode geometries and operating conditions), improvement in electrolyte stability, development of electrode materials more resistant to oxidation, and mitigation of membrane fouling [18–28]. Many of these challenges are not particularly well-suited to laboratory analysis alone, by virtue of the associated financial costs and lengthy timescales. Moreover, as the intrinsically coupled physicochemical processes occur simultaneously in the redox flow batteries including heat and mass transfer, electrochemical reactions, as well as ionic and electronic transfer, it is difficult to experimentally quantify the interrelated parameters that govern the flow batteries. Therefore, numerical modeling that incorporates coupled heat/mass transport and electrochemical kinetics becomes essential to gain a better understanding of flow batteries and to shorten the design and optimization cycles.

To obtain a general overview of modeling treatments on flow batteries, this paper summarizes the various issues associated with flow batteries, and presents a critical review on the numerical investigations of each issue.

The remainder of this paper is organized as follows: i) Section 2 introduces the general principles of the five kinds of flow batteries and the physical/chemical processes during operating the flow batteries; ii) Section 3 shows the governing equations and the derivations of key transport properties for porous-medium models; iii) Section 4 reviews the applications of the lattice Boltzmann method; iv) Section 5 reviews the molecular dynamics and density function simulations for flow batteries; v) Section 6 reviews stack-level network modeling works, and vi) Section 7 summarizes the review and presents a brief discussion about the future investigation directions of flow battery modeling.

2. General description of physical and chemical processes in flow batteries

In a typical redox flow battery system shown in Fig. 1, the reactions occur at the two electrodes can be expressed as:

Positive electrode:

$$C^n - ye^- \underset{\text{Discharge}}{\overset{\text{Charge}}{\rightleftharpoons}} C^{n+y} \tag{1}$$

Negative electrode:

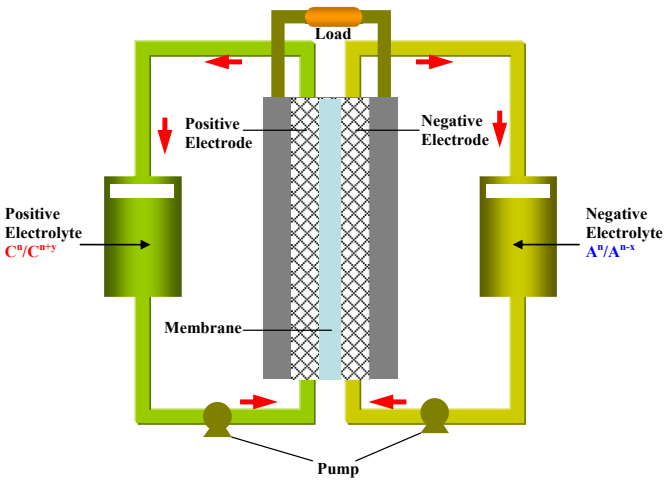

Fig. 1. Schematic of a flow battery system.

$$A^{n-x} + xe^- \underset{\text{Discharge}}{\overset{\text{Charge}}{\rightleftharpoons}} A^n \quad (2)$$

The selection of active species for the positive and negative electrode reactions influences system choices such as electrode material, electrolyte composition, membrane material, and cell design. Various flow batteries can be envisaged and determined by the electrode reactions shown in Fig. 2.

Currently, there are several types of commonly available flow batteries. A brief introduction of each flow battery is provided here and the physical and chemical processes within the flow batteries are thereafter discussed.

2.1. All-vanadium redox flow battery (VRFB)

The VRFB was developed at the University of New South Wales, by Maria Skyllas-Kazacos and co-workers [29,30]. It is a classical, membrane-divided redox flow battery exploiting the ability of vanadium to exist in 4 different oxidation states. Due to this unique property, the battery only has one electroactive element instead of two. By employing the same element in both half-cells, any cross contamination would be avoided, allowing the lifetime of the electrolyte to be extended indefinitely [31]. The charge–discharge reactions for both half-cells are shown as follows:

Positive electrode : $$VO^{2+} + H_2O - e^- \underset{\text{Discharge}}{\overset{\text{Charge}}{\rightleftharpoons}} VO_2^+ + 2H^+ \quad (3)$$

$E^0 = +1.00$ V vs. SHE

Negative electrode : $$V^{3+} + e^- \underset{\text{Discharge}}{\overset{\text{Charge}}{\rightleftharpoons}} V^{2+} \quad (4)$$

$E^0 = -0.26$ V vs.SHE

Overall reaction : $$VO^{2+} + V^{3+} + H_2O \underset{\text{Discharge}}{\overset{\text{Charge}}{\rightleftharpoons}} VO_2^+ + V^{2+} + 2H^+ \quad (5)$$

This system has been successfully operated over a temperature range of 10–40 °C [32–35]. The energy density for 1.7 M vanadium electrolytes is approximately 25 Wh/g [32].

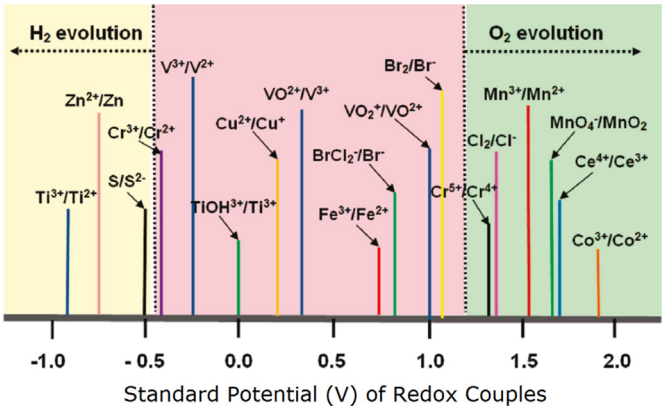

Fig. 2. Possible electrode reactions for redox flow batteries [3].

2.2. Bromide/polysulfide flow battery

Polysulfide/bromide battery (PSB) is a flow battery that uses sodium bromide and sodium polysulfide as salt solution electrolytes. Sodium ions pass through the membrane to maintain the electroneutrality of the cell. PSB has been developed since the early 80s in the UK [36]. Although this technology is labeled as environmentally benign [37], there is concern that toxic bromine vapor can be accidentally released. In this battery, the electrolytes during the discharge cycle are: sodium bromide in the positive side, and sodium polysulfide on the negative side. These chemical species are abundant from the earth, their cost is reasonable and they are very soluble in aqueous solution [38,39], hence the PSB is found to be promising for RFB applications. The cell operating temperature is typically between 20 and 40 °C [36]. The charge–discharge reactions for both half-cells are shown as follows:

Positive electrode : $$3Br^- - 2e^- \underset{\text{Discharge}}{\overset{\text{Charge}}{\rightleftharpoons}} Br_3^- \quad (6)$$

$E^0 = +1.09$ V vs.SHE

Negative electrode : $$S_4^{2-} + 2e^- \underset{\text{Discharge}}{\overset{\text{Charge}}{\rightleftharpoons}} 2S_2^{2-} \quad (7)$$

$E^0 = -0.265$ V vs.SHE

Overall reaction : $$S_4^{2-} + 3Br^- \underset{\text{Discharge}}{\overset{\text{Charge}}{\rightleftharpoons}} 2S_2^{2-} + Br_3^- \quad (8)$$

2.3. Zinc/cerium redox flow cells

The Zn–Ce redox flow battery is a system that combines the very negative zinc couple with a very positive cerium couple to yield an open-circuit voltage that is higher than any of its commercial competitors [40]. It has been under development since the early 1990s by Electrochemical Design Associates Inc [41]. An environmentally benign organic acid is employed as the solvent and a common electrolyte system is used in both half-cells [42]. A Zn/Ce battery containing carbon plastic anodes and platinized titanium mesh cathodes of 100 cm^2 geometrical area separated by a (non-specified type of) Nafion® membrane was patented in 2004 [43]. The charge–discharge reactions for both half-cells are shown as follows:

Positive electrode : $$Ce^{3+} - e^- \underset{\text{Discharge}}{\overset{\text{Charge}}{\rightleftharpoons}} Ce^{4+} \quad (9)$$

$E^0 = +1.28$ V vs.SHE

Negative electrode : $$Zn^{2+} + 2e^- \underset{\text{Discharge}}{\overset{\text{Charge}}{\rightleftharpoons}} Zn \quad (10)$$

$E^0 = -0.76$ V vs.SHE

Overall reaction : $$Zn^{2+} + 2Ce^{3+} \underset{\text{Discharge}}{\overset{\text{Charge}}{\rightleftharpoons}} Zn + 2Ce^{4+} \quad (11)$$

2.4. Soluble lead-acid flow battery

As a metal/metal-oxide flow battery, soluble lead-acid flow battery does not require a membrane; a single active species, Pb^{2+}, is present in the electrolyte. The electrode reactions involve the conversion of the soluble species into solid Pb and PbO_2 phases at the negative and positive electrodes, respectively, during charge and re-dissolution during discharge cycles [44]. Dissolution and deposition of lead is fast and does not usually require over-potentials, however as with conventional lead-acid batteries, hydrogen evolution is observed during the charge cycle at high state-of-charge (SOC), causing a reduced storage capacity [45]. To avoid hydrogen evolution, the methanesulphonic acid is used as the electrolyte [46–48]. The charge–discharge reactions for both half-cells are shown as follows:

$$\text{Positive electrode: } Pb^{2+} + 2H_2O - 2e^- \underset{\text{Discharge}}{\overset{\text{Charge}}{\rightleftharpoons}} PbO_2 + 4H^+ \quad (12)$$

$$E^0 = +1.49 \text{ V vs. } SHE$$

$$\text{Negative electrode: } Pb^{2+} + 2e^- \underset{\text{Discharge}}{\overset{\text{Charge}}{\rightleftharpoons}} Pb \quad (13)$$

$$E^0 = -0.13 \text{ V vs. SHE}$$

$$\text{Overall reaction: } 2Pb^{2+} + 2H_2O \underset{\text{Discharge}}{\overset{\text{Charge}}{\rightleftharpoons}} PbO_2 + Pb + 4H^+ \quad (14)$$

2.5. Iron–chromium redox flow battery

The iron–chromium redox flow battery is one of the first studied flow battery technologies by NASA [49]. Within it, the positive reactant is an aqueous solution of ferric-ferrous redox couple while the negative reactant is a solution of the chromous-chromic couple, both acidified with hydrochloric acid. An ion-exchange membrane is placed between the two half-cells to separate the two electrolytes and to conduct the ions [10]. The charge–discharge reactions for both half-cells are shown as follows:

$$\text{Positive electrode: } Fe^{2+} - e^- \underset{\text{Discharge}}{\overset{\text{Charge}}{\rightleftharpoons}} Fe^{3+} \quad (15)$$

$$E^0 = +0.77 \text{ V vs. SHE}$$

$$\text{Negative electrode: } Cr^{3+} + e^- \underset{\text{Discharge}}{\overset{\text{Charge}}{\rightleftharpoons}} Cr^{2+} \quad (16)$$

$$E^0 = -0.41 \text{ V vs. SHE}$$

$$\text{Overall reaction: } Fe^{2+} + Cr^{3+} \underset{\text{Discharge}}{\overset{\text{Charge}}{\rightleftharpoons}} Fe^{3+} + Cr^{2+} \quad (17)$$

It should be noted that some of these systems considered here are not strictly redox flow batteries because their half-cell reactions involve the deposition of solid species [50]. These systems are also known as “hybrid” redox flow batteries. They are included here because they possess similar designs and operation to the redox flow batteries and are generally categorized under “flow batteries”. Such hybrid systems include those that involve the deposition of a metal at the negative electrode during charge (e.g. the Zinc/cerium and soluble lead-acid batteries).

All the above-mentioned flow batteries (with exception to the soluble lead-acid flow battery which uses the planar plate electrode) utilize porous carbon materials as the electrodes. As illustrated in Fig. 3, the reactants in electrolyte are initially transported from the electrode inlet by diffusion and dispersion (macro-scale) in the bulk, and then to the pore wall by diffusion and convection within a pore space (micro-scale) of the electrode. The reactants are adsorbed onto the electrode pore wall to partake in the electrochemical reactions, then the products are desorbed and diffuse out. Finally, they are dispersed in the electrolyte to cycle back into the reservoir. During operating processes, protons and other charge carriers transfer through the membrane or separator, while electrons transfer through an external load to form an electrical circuit. Heat will be generated due to activation loss of reaction and ohmic resistance, and the produced heat is carried out by the flowing electrolyte.

3. Porous-medium models

3.1. Governing equations

3.1.1. Simplifications and assumptions

The simplifications and assumptions commonly used for abridging the process of solving the numerical models are summarized as follows:

(1) Possible side reactions, such as hydrogen and oxygen evolutions, are not considered.
(2) An isothermal condition is assumed in the entire domain.
(3) The membrane is impermeable to all ions and species, except for protons.
(4) The transport due to ionic interactions in electrolyte is neglected.

3.1.2. Conservation equations for fluid flow

The macroscopic superficial velocity of electrolyte $\vec{u}$ within the porous electrode can be expressed by Darcy's law [51]:

$$\frac{\mu}{K}\vec{u} = -\nabla p \quad (18)$$

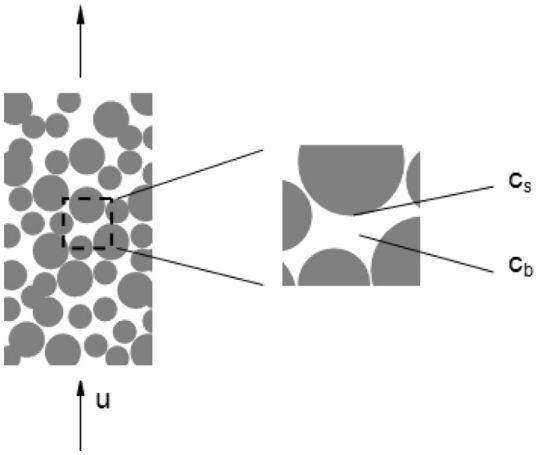

Fig. 3. Schematic of the species transport process within a porous electrode.

where ν is the kinematic viscosity, K is the permeability coefficient and p is pressure. The permeability of a porous medium is a function of the material properties. The constitutive relation and the method in appropriate expression selection for permeability will be discussed in detail in next section.

The liquid pressure is determined from an overall mass balance as:

$$\nabla \cdot \vec{u} = 0 \tag{19}$$

Combining Eqs. (18) and (19) we can obtain:

$$-\frac{K}{\nu\rho}\nabla^2 p = 0 \tag{20}$$

In practical operations, when the SOC is larger than 0.85, side reactions are prone to occur [52,53]. If the side reactions, notably the evolution of oxygen in the positive electrode and the evolution of hydrogen in the negative electrode on charge are considered, the flow equations should be rewritten as:

$$\vec{u}_l = -K\frac{k_{rl}}{\mu_l}\nabla p_l \quad \text{(liquid phase)} \tag{21}$$

$$\vec{u}_g = -K\frac{k_{rg}}{\mu_g}\nabla p_g \quad \text{(gas phase)} \tag{22}$$

where the subscripts "l" and "g" represent the properties of liquid and gas phases, k_r is the relative permeability of a phase and is a function of phase saturation alone.

The difference between the pressures of gas phase and liquid phase is related to capillary pressure:

$$p_c = p_g - p_l = \sigma \cos\theta_c(\varepsilon/K)^{0.5}J(s) \tag{23}$$

where $J(s)$ represents the Leverette function and s represents the liquid saturation in a porous medium.

The liquid-phase and gas-phase velocities are related by the slip velocity $\vec{u}_{slip}$ in the following manner:

$$\vec{u}_{slip} = \vec{u}_g - \vec{u}_l \tag{24}$$

An equation for the slip velocity can be derived by performing a balance of force on a bubble and the final form can be expressed as [53]:

$$\vec{u}_{slip} = \frac{d_b^2}{18\mu_l}\nabla p \tag{25}$$

where d_b is the bubble diameter.

3.1.3. Conservation equations for mass transport

The transport equation for ion i in the electrolyte is:

$$\frac{\partial c_i}{\partial t} = \nabla\cdot\left(D_i^{eff}\nabla c_i\right) + \frac{Fz_i}{RT}\nabla\cdot\left(D_i^{eff}c_i\nabla\phi_s\right) - \nabla\cdot(\vec{u}c_i) + S_i \tag{26}$$

where D_i^{eff} is the effective diffusivity for species i in porous electrode and S_i is the source term due to chemical/electrochemical reactions. The effective diffusivity consists of the stagnant and the dispersion diffusivity and is constructed as follows [54,55]:

$$D_i^{eff} = (0.6 \sim 0.8)D_i + 0.1d_p u \tag{27}$$

or [94]:

$$\frac{D^{eff}}{D} = \varepsilon^{1.1}\left(1 + 1.46\times 10^{-3}\mathrm{Pe}^2\right) \tag{28}$$

where D_i is the intrinsic diffusivity of species i and d_p is the pore diameter.

Within a pore space of the electrode, the rate of mass transfer of the reactants (or products) to (or from) the pore wall can be expressed as:

$$N_i = k_m(c_i - c_i^s) \tag{29}$$

where c_i^s is the pore wall concentration, c_i is the bulk concentration in the pore space and k_m is the local mass transport coefficient. k_m is related to the morphology of pore wall, electrolyte property and the local velocity of electrolyte.

Corresponding to the third item of the simplifications and assumptions, when a proton is the only mobile ion through the membrane, the mass conservation equation is:

$$\vec{N}_{H^+} = -\frac{\sigma_{mem}}{F}\nabla\phi_{mem} \tag{30}$$

where σ_{mem} and ϕ_{mem} are the conductivity and electronic potential of the ion-exchange membrane, respectively.

However, in practical operations the ion crossover through the membrane is inevitable, which results in the loss of energy capacity. The works on modeling the effect of ions crossover through the membrane will be discussed in Section 3.2.

3.1.4. Conservation equations for heat transport

The energy balance takes into account heat conduction, convective heat transport and heat generation by electrochemical reaction and Joule heating. As a reasonable approximation, it is assumed that the liquid and solid phases in the electrodes attain the same temperature. The energy balance is expressed as [56]:

$$\frac{\partial}{\partial t}\left(\overline{\rho C_p}T\right) + \nabla\cdot\left(\vec{u}\,\overline{\rho C_p}T\right) = \bar{\lambda}\nabla^2 T + \sum_k Q_k \tag{31}$$

where $\overline{\rho C_p}$ is the volume-averaged thermal capacity, $\bar{\lambda}$ is the volume-averaged thermal conductivity and Q_k is the source term (See Table 1).

It is worth pointing out that the second item of the simplifications and assumptions in Section 3.1 is only valid for the case when both the reservoir and flow rate are sufficiently large. Otherwise, the isothermal condition cannot be maintained and the thermal effect during operation should be taken into account.

3.1.5. Electrochemical kinetics

Although the Butler–Volmer equation can be applied to most of the electrochemical reactions, due to the different reactants and reaction environments for different kinds of flow batteries, the formulations describing the electrochemical kinetics are listed by respective type of flow battery.

Table 1
Sources for the energy equation. They are, from top to bottom, heating by activation losses, electrochemical reaction and Joule heating [56].

Term	Membrane	−ve Electrode	+ve electrode
Q_{act}	0	$\eta_1\nabla\cdot\vec{j_1}$	$\eta_2\nabla\cdot\vec{j_2}$
Q_{rev}	0	$-\Delta S_1 T\nabla\cdot\vec{j_1}/F$	$\Delta S_2 T\nabla\cdot\vec{j_2}/F$
Q_{ohm}	$\sigma_{mem}^{eff}\lvert\nabla\phi\rvert^2$	$\sigma_s^{eff}\lvert\nabla\psi\rvert^2 + \sigma_e^{eff}\lvert\nabla\phi\rvert^2$	$\sigma_s^{eff}\lvert\nabla\psi\rvert^2 + \sigma_e^{eff}\lvert\nabla\phi\rvert^2$

◆ All vanadium redox flow battery

The electrochemical reactions taking place on the solid surfaces of the porous graphite electrode can be expressed using the Butler–Volmer equation as [57,58]:

$$j_1 = \varepsilon A_v F k_1 \left(c^s_{V(III)}\right)^{\alpha_{-,1}} \left(c^s_{V(II)}\right)^{\alpha_{+,1}} \left\{ \exp\left(\frac{\alpha_{+,1} F \eta_1}{RT}\right) - \exp\left(-\frac{\alpha_{-,1} F \eta_1}{RT}\right) \right\} \tag{32}$$

and

$$j_2 = \varepsilon A_v F k_2 \left(c^s_{V(V)}\right)^{\alpha_{-,2}} \left(c^s_{V(IV)}\right)^{\alpha_{+,2}} \left\{ \exp\left(\frac{\alpha_{+,2} F \eta_2}{RT}\right) - \exp\left(-\frac{\alpha_{-,2} F \eta_2}{RT}\right) \right\} \tag{33}$$

Eqs. (32) and (33) are for the negative and positive electrodes, respectively, where A_v is specific surface area of the porous electrode, k_1 (1.7E−7 m s^{-1}) and k_2 (6.8E−8 m s^{-1}) are the standard rate constants for negative and positive electrochemical reactions, $c^s_i, i \in \{V^{2+}, V^{3+}, VO^{2+}, VO_2^+\}$ are the vanadium species concentrations at the liquid–solid interfaces of the porous region, α_+ and α_- are the anodic and cathodic transfer coefficients, η_1 and η_2 are the overpotentials in the negative and positive electrodes, respectively.

The interface concentrations c^s_i can be related to the bulk concentrations c_i by balancing the electrochemical reaction rate with the rate of mass transfer of the reactants to (or from) the electrode surface. For the negative electrode during discharge, the balance is:

$$k_{m1}\left(c_{V(II)} - c^s_{V(II)}\right) = \varepsilon k_1 \left[c^s_{V(II)} \exp\left(\frac{\alpha_{+,1} F \eta_1}{RT}\right) - c^s_{V(III)} \exp\left(-\frac{\alpha_{-,1} F \eta_1}{RT}\right) \right] \tag{34}$$

and

$$k_{m1}\left(c_{V(III)} - c^s_{V(III)}\right) = \varepsilon k_1 \left[c^s_{V(III)} \exp\left(\frac{\alpha_{-,1} F \eta_1}{RT}\right) - c^s_{V(II)} \exp\left(-\frac{\alpha_{+,1} F \eta_1}{RT}\right) \right] \tag{35}$$

where k_m is the local mass transfer coefficient and can be approximated by Ref. [59]:

$$k_m = 1.6 \times 10^{-4} \vec{u}^{0.4} \tag{36}$$

Combining Eqs. (34) and (35), the concentrations of $V(II)$ and $V(III)$ at the liquid–solid interface can be obtained.

◆ Soluble lead-acid flow battery

The soluble lead-acid battery is a redox flow cell that uses a single reservoir to store the electrolyte and does not require a micro-porous separator or membrane, allowing a simpler design and a substantial reduction in cost. The redox reactions for the Pb/Pb(II) and PbO_2/Pb(II) electrodes were described in the Butler–Volmer expressions [60]:

$$j_{Pb} = F k^0_{Pb} c_{Pb(II)} \left[\exp\left(\frac{F\eta^-}{RT}\right) - \exp\left(-\frac{F\eta^-}{RT}\right) \right] \tag{37}$$

$$j_{PbO_2} = F k^0_{PbO_2} c_{Pb(II)} \left(\frac{c_{H^+}}{c^0_{H^+}}\right) \left[\exp\left(\frac{F\eta^+}{RT}\right) - \exp\left(-\frac{F\eta^+}{RT}\right) \right] \tag{38}$$

Eqs. (37) and (38) are for the negative and positive electrodes, respectively, where k^0_{Pb}(2.1E−7 m s^{-1}) and $k^0_{PbO_2}$(2.5E−7 m s^{-1}) are the standard rate constants for negative and positive electrochemical reactions.

◆ Polysulfide/bromide flow battery

The redox reactions for the PSB are shown in Eqs. (6) and (7). The overpotentials resulting at each electrode was determined by inverting the Butler–Volmer equation in the numerical simulation by Scamman et al. [61]. The electrochemical kinetics is expressed as:

$$i = \frac{\exp[(\alpha_a zF/RT)\eta] - \exp[(-(\alpha_c zF/RT)\eta]}{1/i_0 + (1/i_{La})\exp[(\alpha_a zF/RT)\eta] - (1/i_{Lc})\exp[-(\alpha_c zF/RT)\eta]} \tag{39}$$

where i_0 ($i_0 = zFk_s c_{reac}$, with the kinetic rate constant k_s = 4.0E−7 m s^{-1}) is the exchange current density, i_{La} and i_{Lc} are the anodic and cathodic limiting current densities.

◆ Fe/Cr redox flow battery

Fedkiw and Watts [62] carried out a mathematical model for the Iron/Chromium redox flow battery. The electrochemical kinetics can be expressed as:

$$i^{n,total}_{Fe} = i^n_{Fe} = i^{0,f}_{Fe}\left\{ \left(Fe^{2+,s}/Fe^{2+,f}\right)\exp\left[\frac{F}{RT}\alpha^A_{Fe}(\phi_{m,Fe} - \phi_{s,Fe})\right] - \left(Fe^{3+,s}/Fe^{3+,f}\right)\exp\left[-\frac{F}{RT}\alpha^C_{Fe}(\phi_{m,Fe} - \phi_{s,Fe})\right]\right\} \tag{40}$$

$$\begin{aligned} i^{n,total}_{Cr} = i^n_{Cr} + i^n_{H_2} = {} & i^{0,f}_{Cr}\left\{ (Cr^{2+,s}/Cr^{2+,f})\exp\left[\frac{F}{RT}\alpha^A_{Cr}(\phi_{m,Cr} - \phi_{s,Cr})\right] - (Cr^{3+,s}/Cr^{3+,f})\exp\left[-\frac{F}{RT}\alpha^C_{Cr}(\phi_{m,Cr} - \phi_{s,Cr})\right]\right\} \\ & + i^0_{H_2}\left\{ \exp\left[\frac{F}{RT}\alpha^A_H(\phi_{m,Cr} - \phi_{s,Cr} - U_{AH})\right] - \exp\left[-\frac{F}{RT}\alpha^C_H(\phi_{m,Cr} - \phi_{s,Cr} - U_{AH})\right]\right\} \end{aligned} \tag{41}$$

where

$$i^{0,f}_{Fe} = i^{0,ref}_{Fe}(Fe^{2+,f}/Fe^{2+,ref})^{\alpha^C_{Fe}}(Fe^{3+,f}/Fe^{3+,ref})^{\alpha^A_{Fe}} \tag{42}$$

$$i^{0,f}_{Cr} = i^{0,ref}_{Cr}(Cr^{2+,f}/Cr^{2+,ref})^{\alpha^C_{Cr}}(Cr^{3+,f}/Cr^{3+,ref})^{\alpha^A_{Cr}} \tag{43}$$

with the superscripts s, f and ref denoting the pore wall surface, feed condition and reference values ($i^{0,ref}_{Fe}$=7.5 mA cm^{-2}, $i^{0,ref}_{Cr}$ = 50 mA cm^{-2}), respectively. U_{AH} is the open-circuit potential difference between H_2 and Cr reaction, and it depends on the SOC.

3.1.6. Constituent relationships and physicochemical properties

The constitutive relationships used in modeling flow batteries are listed in Table 2. The method employed to choose appropriate constituent relationships in modeling flow batteries is discussed in Section 4.

Table 2
Constitutive relations.

Parameters	Expressions
Capillary pressure	$p_c = p_g - p_l = \sigma cos\theta_c(\varepsilon/K)^{0.5}J(s)$
	$J(s) = \begin{cases} 1.417(1-s) - 2.120(1-s)^2 + 1.263(1-s)^3 \\ 1.417s - 2.120s^2 + 1.263s^3 \end{cases}$
	$0 < \theta_c \le 90^\circ$
	$90^\circ < \theta_c < 180^\circ$
Permeability	$K = \frac{d_f^2\varepsilon^3}{K_{CK}(1-\varepsilon)^2}$ (One of the commonly used expressions)
Relative permeabilities	$k_{rl} = s^3$
	$k_{rg} = (1-s)^3$
Effective diffusion coefficient	$D^{eff}/D = \varepsilon^{1.1}(1 + 1.46 \times 10^{-3}\mathrm{Pe}^2)$
Nernst–Planck equation	$\vec{N}_i = -D_i^{eff}\nabla c_i - Fz_i c_i \mu_i \nabla\phi_s + \vec{u}c_i$
Electrically neutral condition	$\sum_i z_i c_i = 0$
Total current density in the electrolyte	$\vec{i} = \sum_i \vec{i}_i = -F\sum_i z_i D_i^{eff}\nabla c_i - F^2\sum_i z_i^2 c_i \mu_i \nabla\phi_s$
Effective electronic conductivity	$\sigma_m^{eff} = (1-\varepsilon)^{1.5}\sigma_m$
Nernst equation of electrochemical potential	$E = E^0 - \frac{RT}{nF}\ln\frac{\prod a_{product}^{v_i}}{\prod a_{reac\ tan\ t}^{v_i}}$

The expression of Nernst–Planck equation in Table 2 corresponds to the fourth item of the simplifications and assumptions. It is only valid in the use of dilute electrolyte where the ionic interactions are weak. In fact, it has been observed in experiments that these coefficients can be significant in comparison to the chemical drag coefficient [63]. Also, neglecting these cross-coefficients hampers the applicability of the Nernst–Planck equation in ion-exchange membranes and multi-ionic non-dilute solutions [64]. The effect of ionic interactions will be discussed in Section 3.2.

The physicochemical properties for the components in redox flow batteries are listed in Table 3.

According to the concept of the different length scales of the processes in flow batteries, the solution for modeling flow batteries includes three stages (See Fig. 4) of exploration [57]:

- distribution of the pressure and of the flow velocity in cell;
- distribution of the chemical species concentrations in the cell taking account of electrochemical interaction;
- distribution of the electric field and the current density within the cell.

In addition, the soluble lead-acid flow battery utilizes the planar electrode (non-porous), thus the velocity distribution should be solved using the Navier–Stokes equation. The remaining stages are the same as the illustration in Fig. 4.

Table 3
Physicochemical properties.

Parameters	Symbols	Value	Unit	Reference
Proton diffusivity in membrane	$D_{H^+}^{\mathrm{eff}}$	3.5×10^{-10}	$m^2\ s^{-1}$	[65]
Electrolyte kinematic viscosity	ν	1.0×10^{-6}	$m^2\ s^{-1}$	
Conductivity of the solid phase	σ_m	1000	$S\ m^{-1}$	
Conductivity of the membrane	σ_{mem}	10	$S\ m^{-1}$	
Specific surface area	A_r	2×10^5	m^{-1}	[20]
Polymer electrolyte membrane	δ_{mem}	1.8×10^{-4}	M	
Operating temperature	T	300	K	
Electrode porosity	ε_0	0.7		
Electrode fiber diameter	d_f	17.6	Mm	[20]
Anodic transfer coefficient	$\alpha_{+,1}$	0.5		
Cathodic transfer coefficient	$\alpha_{-,2}$	0.5		
Equivalent weight of ionomer	EW	1.1	$kg\ mol^{-1}$	[66]
Dry membrane density	ρ_{mem}	1980	$kg\ m^{-3}$	[67]

3.2. Determinations of transport properties

The complex processes including fluid flow, mass transport, heat transport and electrochemical kinetics within a flow battery are strongly coupled [68]. Some key parameters, such as permeability of the porous electrode, effective diffusivities of ions through the porous electrode, ions diffusivities through the membrane, the electrolyte viscosity and ionic interaction coefficients in the electrolyte, play significant roles on the coupled processes and affect the performance of redox flow batteries. In this section, past work on the determination and selection of the key parameters are reviewed and their effect on the variable distribution and cell performance is discussed.

3.2.1. Transport properties through porous electrodes

In most flow batteries, porous materials are used as electrodes where the electrochemical reactions occur. In such batteries, the reactants pass through the porous electrodes and take part in the reactions at the pore surfaces of the electrodes. The specific surface area of the pore controls the rate of reactions. The flow resistance is governed by the pore size distribution and the permeability of the porous electrodes [69].

As an important parameter for modeling flow within the porous media, the permeability K depends on both the tortuosity of the pore space and the pore size. In fact, K has the dimension of area and can be considered as a representative of the cross section of an effective channel for fluid flow through the pore space. Table 2 shows a commonly used expression of K in which K_{CK} is the Kozeny–Carman factor. K_{CK} is found to be a function of porosity, particularly in the high porosity range of fibrous media [70].

From the literature, the methods in the determination of the permeability K include: (a) qualitatively describing the behavior of the permeability as a function of porosity, without any attempt to provide specific correlations [71]; (b) using an Ergun-like relationship including the equivalent particle diameter and an empirical constant [72], even taking into account of slip flow by including a linear or second order Knudsen number dependence [73,74]; (c) assuming a uniform geometrical cell structure or using some reduced geometrical model of the cell [75]. However, it was reported that none of the methodologies mentioned translated well in practice [76]. An alternative way to determine the permeability K of porous material is using numerical simulation.

It has been well established that fine scale heterogeneities exist in the porous structure, but the best way to incorporate this fine scale data into large scale flow simulation models remains unclear. Specifically, averaging techniques are needed to scale up the fine scale permeability to the larger scales appropriate for flow simulation and engineering calculations. If the scale over which the averaged permeability is defined, is large relative to the scale of heterogeneity within the porous medium, the permeability is referred to as an effective permeability, which is a property of the medium and does not vary with the flow conditions to which the medium is subjected. Otherwise, if the larger scale does not encompass all the scales of variation of the permeability field, the averaged permeability is referred to as an equivalent permeability, which is not a constant property of the medium. Rather, some variations in the equivalent permeability under different flow conditions are typically expected [77].

White and Horne [78] presented a numerical technique for the determination of equivalent permeability tensor that entails the use of several different sets of boundary conditions and the subsequent averaging of the coarse scale permeability results.

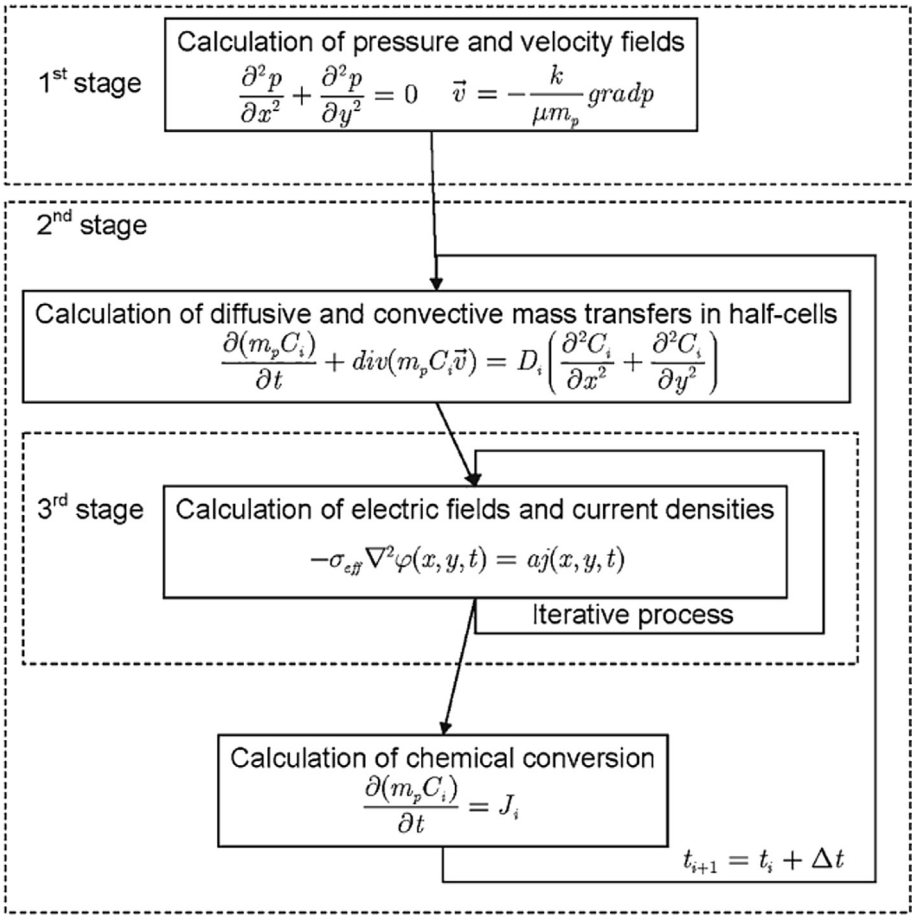

Fig. 4. The flowchart for modeling flow batteries [57].

However, their method is limited in that the resulting averaged equivalent permeability is not in general a symmetric tensor. Durlofsky [79] proposed a numerical model to determine the equivalent permeability for heterogeneous porous media. The method entails solution of the fine scale pressure equation subject to periodic boundary conditions to yield the coarse scale or equivalent grid block permeability. When the region over which this coarse scale permeability is computed constitutes a representative elementary volume (REV), the resulting equivalent permeability may be interpreted as the effective permeability of the region. In addition, there have been great interest in understanding the relationship between the transport of viscous fluids and other transport processes such as electrical conduction and diffusion-limited trapping [80,81]. Each of these processes can be used to estimate the permeability of a porous media [82–85]. Specially, Schwartz et al. applied a numerical study based on two lengths—one derived from electrical conduction and the other derived from immiscible displacement—and found the estimates of permeability were more reliable than those based on rigorous bounds related to pore space diffusion [85].

In addition, to performing the numerical modeling, a key transport property – the effective diffusivity in the porous electrode – needs to be accurately determined. A simple method is to correlate it against the intrinsic diffusivity and the porosity of the porous material by using a Bruggemann correction [86], which is widely used in previous models [87–89]. However, this correlation misses the effect of different structures of porous material, namely, fibers or particles. Alternatively, the effective diffusivity can be determined using experimental methods. The UV/V spectroscopic measurements are used to determine the amount of a specific ion transporting through a porous material separating two reservoirs. The diffusivity of the ion is calculated based on the porous media area, thickness and the overall solution volume [90–92]. Nevertheless, a major problem associated with this method is that the dispersion effect, which affects the mass transport, has been ignored. Recently, Pant et al. [93] proposed a 'diffusion bridge' configuration to simulate the transport process in flow batteries. The flow of electrolytes in two channels separated by the porous diffusion bridge includes the dispersion effect. The amount of ion diffused through the diffusion bridge was determined by the ion-chromatography measurements. Unfortunately, their method suffered from a complicated setup and a lengthy testing time. Alternatively, the effective diffusivity in the porous electrode of a VRFB was electrochemically determined by Xu and Zhao by using a uniquely proposed setup [94], as shown in Fig. 5. The dispersion effect on effective diffusivity was included (See Fig. 6) and it was found that dispersion played a significant role, especially at high flow rates.

A steady-state two-dimensional mass transport and electrochemical reaction model for VRFB was developed with the dispersion effect included in the effective diffusivity through the porous electrode [95]. The numerical results indicate that due to the small effective diffusivities of vanadium ions through the porous electrode, the dispersion effect is not significant at low flow rates. Increasing the flow rate enhances the dispersion effect; but compared with the increase rate of the dispersion effect, the increase rate of the convection effect with the flow rate is faster, making the convective transport predominate at high flow rates. It

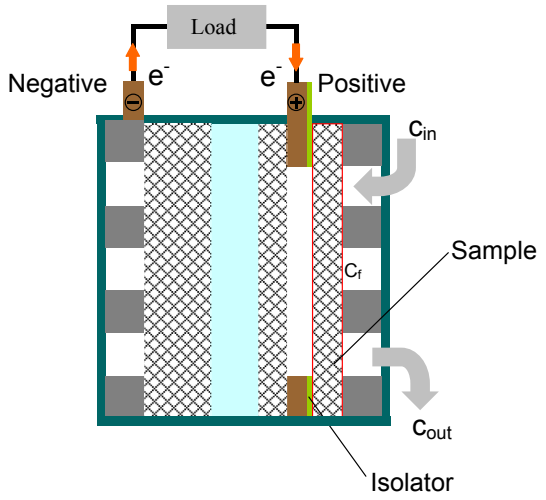

Fig. 5. Schematic of a setup for the determination of the effective diffusivity in porous media [94].

is also suggested that if the intrinsic diffusivities of vanadium ions in a certain electrolyte are much larger than those in the sulfuric acid-based system, there would be marked improvement in the cell performance under the same electrolyte flow rate.

3.2.2. Ions transport properties through membranes

Almost all rechargeable batteries exhibit energy capacity loss after long term charge–discharge cyclings. There are several reasons responsible for energy capacity decay in rechargeable batteries, with 'self-discharge', i.e. crossover of ions through the membrane, as the most notable reason [96–100]. The crossover flux can be expressed as:

$$\vec{N}_{i,mem} = -D^{eff}_{i,mem}\nabla c_i - Fz_i c_i \frac{D^{eff}_{i,mem}}{RT}\nabla\phi_{mem} - \frac{K_{mem}}{\nu M_i}\nabla p \qquad (44)$$

where the first, second and third terms on the right-hand side represent the diffusion flux, migration flux and convection flux, respectively, with subscript "*mem*" the properties related with membrane. The diffusion rate is determined by the species concentration gradient across the membrane, the migration rate is determined by the electric field effect, and the convection rate by the pressure difference between two sides of the membrane.

Consider a VRFB, once the crossover of vanadium ions through the membrane is taken into account, the reactions between vanadium ions with different electrovalences should be involved.

In the positive electrolyte:

$$2VO_2^+ + V^{2+} + 2H^+ \rightarrow 3VO^{2+} + H_2O \qquad (45)$$

$$VO_2^+ + V^{3+} \rightarrow 2VO^{2+} \qquad (46)$$

$$VO^{2+} + V^{2+} + 2H^+ \rightarrow 2V^{3+} + H_2O \qquad (47)$$

In the negative electrolyte:

$$V^{2+} + VO^{2+} + 2H^+ \rightarrow 2V^{3+} + H_2O \qquad (48)$$

$$2V^{2+} + VO_2^+ + 4H^+ \rightarrow 3V^{3+} + 2H_2O \qquad (49)$$

$$V^{3+} + VO_2^+ \rightarrow 2VO^{2+} \qquad (50)$$

Thus far, few works have been carried out to numerically simulate the self-discharge process in VRFBs. You and Zhang [88] established a simple mathematical model and found that the diffusion rate of vanadium ions depended on the diffusion coefficient and the concentration gradient between the two half-cells. They studied two operating conditions, i.e. the initial SOC was 0 and 0.65, respectively, and found that there were two obvious changes in the diffusion flux of vanadium ions, corresponding to the vanishing time of VO_2^+ and V^{2+} respectively. Tang and Skyllas-Kazacos [100] developed a dynamic model based on mass balance for each of the four vanadium ions in the VRFB electrolyte in conjunction with the Nernst Equation. Ions across the membrane along with side reactions were taken into account. The performances of three different membranes (Selemion CMV, Selemion AMV and Nafion 115) were studied (See Fig. 7) and operational issues, such as pumping pressure and electrolyte flow rate, were analyzed and discussed. This model can be used to determine when periodic electrolyte remixing or rebalancing should take place to restore cell capacity and achieve optimal operation. After that, they modeled the concentration profiles of different vanadium ions as a function of time under different charge and discharge currents [101]. In the case of cation exchange membranes, a build-up in total vanadium ion concentration in the positive half-cell was predicted. The effects of factors other than diffusion were discussed in detail, along with electrolyte maintenance strategies to restore capacity during long term operation. More recently, they further incorporated the effect of self-discharge reactions into a thermal model for the purpose of electrolyte temperature control [102]. Simulation results showed that the incorporated model can be used to investigate the thermal effect of the self discharge reactions on both continuous charge–discharge cycling and during standby periods, and can help optimize battery designs and fabrication for different applications.

Due to the viscosity difference between anolyte and catholyte, at an operating condition of constant flow rate (i.e. with same flow rate in each half-cell), a pressure difference exists between two sides of the membrane, which results in the convective transport of species across the membrane. A comprehensive model was developed by Kumbur et al. for the first time [103], incorporating the transport of all species through the membrane as a result of diffusion, migration and convection. The model results suggested that diffusion and migration may not be the dominating mechanisms for species crossover in the membrane. Motivated by this

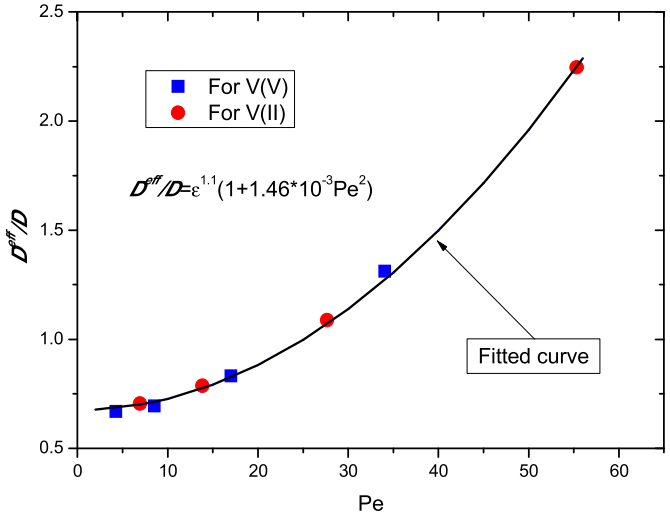

Fig. 6. Mass-transfer correlation, D^{eff}/D vs. Pe [94].

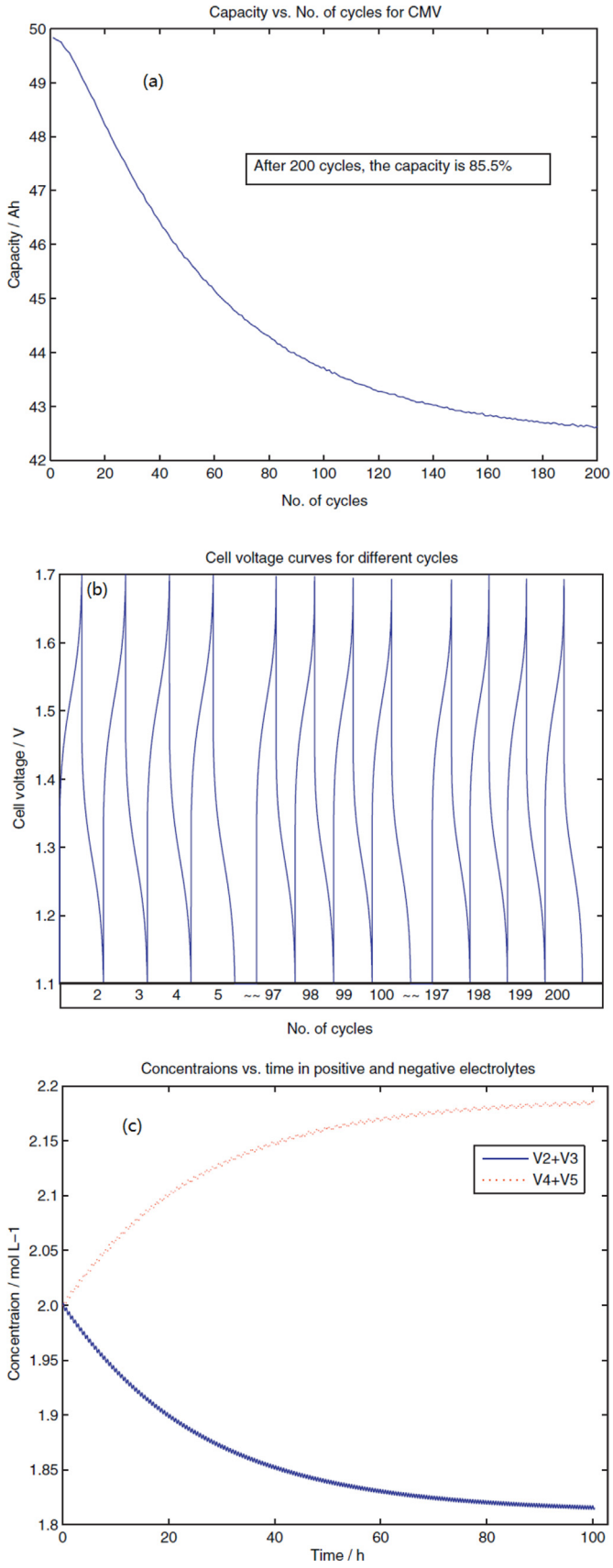

Fig. 7. (a) Capacity vs. number of cycles for 200 cycles for CMV membrane; (b) comparison of cell voltage curves for different cycles for CMV membrane; (c) Concentrations of positive and negative electrolytes vs. time for 200 cycles for CMV membrane [101].

observation, the same authors investigated the convective transport and related effects on the vanadium ions crossover by numerical simulation [104]. The direction and magnitude of the convection transport and resulting crossover is found to be highly dependent on the viscosity of the electrolytes in each half-cell, as shown in Fig. 8. They also proposed to operate the flow battery at a condition of constant pressure (i.e. same pressure in each half-cell but the flow rates are different) to reduce the impact of convection.

3.2.3. Transport properties of electrolytes

(1) The change of electrolyte viscosity with SOC

The viscosity of the electrolyte in a flow battery is an important factor in determining the pressure drop through the electrode as well as the local velocity. For flow batteries, the concentrations of ions in the electrolyte fluctuate periodically with SOC during the charge–discharge cycles. This causes a variation in the viscosity of the electrolyte. For example, in a VRFB, changes in the concentrations of V^{2+}, VO_2^+, V^{3+}, VO^{2+} and H^+ ions during the charge process can be illustrated in Fig. 9.

Hu et al. [106,107] used the Eyring's absolute rate theory and the semi-ideal hydration model to study the mixing behavior of viscosities of electrolyte solutions under isopiestic equilibrium for the first time. The basic idea is to predict the viscosity of the mixed electrolyte from using the viscosities of binary solutions (i-H_2O). From Eyring's absolute rate theory, for the electrolyte solution, the viscosity can be expressed as:

$$\ln \nu_{mix} = \sum_i x_i \ln \nu_i^{pure} + x_w \ln \nu_w^{pure} + \frac{1}{RT}\Delta G^{\neq} \tag{51}$$

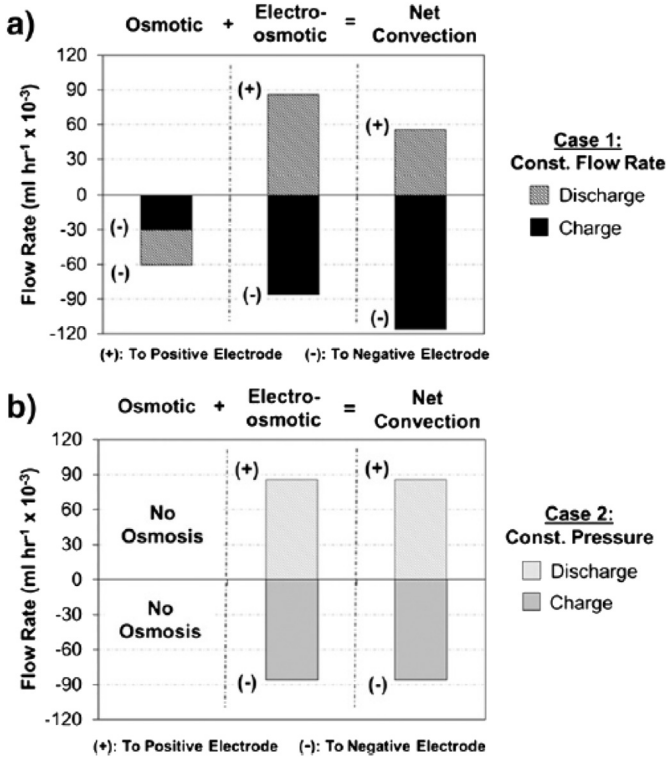

Fig. 8. Average convective flow rate across the membrane during the 35th cycle at 50% SOC for a) Case 1 (constant flow rate) and b) Case 2 (constant pressure) [104].

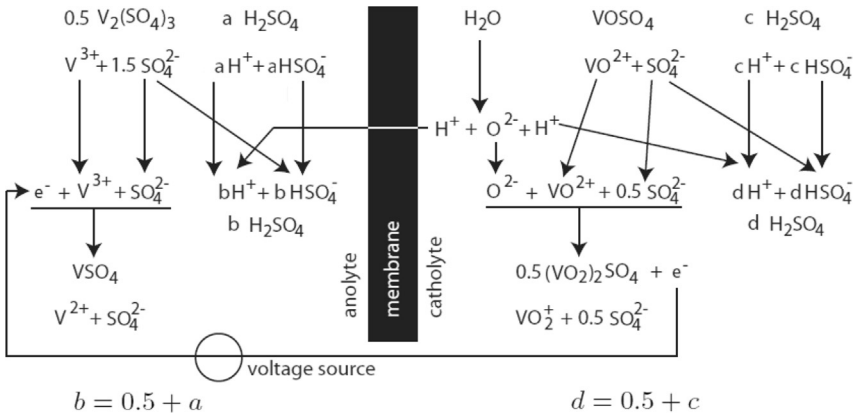

Fig. 9. Illustration of anolyte and catholyte component and concentration variations from SOC = 0 to SOC = 1 [108].

where ν is kinematic viscosity and x_i is the molar fraction,

$$x_i = m_i \Big/ \left((1000/M_w) + \sum_{i=1}^{n} m_i \right) \tag{52}$$

with m_i the molality (mol/kg);and $\Delta G^{\neq}$ is the molar excess activation free energy,

$$\Delta G^{\neq} = \beta RT \sum z_i x_i \ln a_i \tag{53}$$

where β is a system-specific constant for non-ideal solutions, z_i and a_i are the stoichiometric coefficient and activity of the component.

For a binary solution, the viscosity can be expressed as:

$$\ln \nu_i^{(i,0)} = x_i^{(i,0)} \ln \nu_i^{pure} + x_w^{(i,0)} \ln \nu_w^{pure} + \frac{1}{RT} \Delta G_i^{\neq (i,0)} \tag{54}$$

where the variables with the superscript (i, 0), together with the subscript i denote the quantities of i in the binary solution (i-H_2O) having the same water activity as that of a mixed solution. Those without the superscript (i, 0) denote the corresponding quantities in the mixed solution.

Combing Eqs. (50) and (52) and (53), the viscosity of the electrolyte can be expressed as:

$$\ln \nu_{mix} = \sum_i \frac{x_i}{x_i^{(i,0)}} \ln \nu_i^{(i,0)} + \beta \sum_i z_i x_i \ln \left(\frac{z_i m_i}{\sum_i z_i m_i} \right) \tag{55}$$

or

$$\ln \mu_{mix} = \sum_i \frac{x_i}{x_i^{(i,0)}} \ln \mu_i^{(i,0)} + \beta \sum_i z_i x_i \ln \left(\frac{z_i m_i}{\sum_i z_i m_i} \right) \tag{56}$$

According to Eq. (55), together with the experimental data for the relationships between the dynamic viscosity and concentration for VSO_4, $V_2(SO_4)_3$, $VOSO_4$ and $(VO_2)_2SO_4$ solutions [105,108], one can obtain the expressions for viscosities of anolyte and catholyte in VRFB. Based on these results, the effects of viscosity change with SOC on the pressure drop, cell performance and system efficiency were investigated by Xu and Zhao [108], and the results are shown in Fig. 10. The comparison between the present model and the simplified model with constant-viscosity indicates that the consideration of the SOC-dependent electrolyte viscosity enables i) a more realistic simulation of the distributions of overpotential and current density in the electrodes, and ii) more accurate estimations of pumping work and the system efficiency of VRFBs.

(2) Ionic interactions in electrolytes

As mentioned above, the commonly used Nernst–Planck equation (See Table 2), in its basic form, ignores the transport due to ionic interactions, i.e. it neglects the cross-coefficients. However, it has been observed that in experiments these coefficients can be significant in comparison to the chemical drag coefficient when the electrolyte becomes non-dilute [63]. Hence, the effect of ionic interactions is indispensable in a comprehensive expression. The flux term $\vec{N}_i$ including the contributions from the independent motion of ion i and the interaction of this ion with other ions can be expressed as:

$$\vec{N}_i = -D_i^{eff} \nabla c_i - F z_i c_i \frac{D_i^{eff}}{RT} \nabla \phi_s + \vec{u} c_i - \sum_{k=1, k \neq i}^{n} L_{ik} \nabla \mu_k \tag{57}$$

where the first, second, third and fourth terms in the right-hand side represent the diffusion flux, migration flux, convection flux and the flux by ionic interaction effect, respectively, with μ_k the chemical potential of ion k, L_{ik} the cross-coefficient representing the drag on species i due to the thermodynamic force from ion k. Then the transport equation for ion i is:

$$\begin{aligned} \frac{\partial c_i}{\partial t} = {} & \nabla \cdot \left(D_i^{eff} \nabla c_i \right) + \frac{F z_i}{RT} \nabla \cdot \left(D_i^{eff} c_i \nabla \phi_s \right) - \nabla \cdot (\vec{u} c_i) \\ & + \nabla \cdot \left(\sum_{k=1, k \neq i}^{n} L_{ik} \nabla \mu_k \right) + S_i \end{aligned} \tag{58}$$

where S_i is the source term due to electrochemical/chemical reactions.

The cross-coefficient L_{ik} is relatively difficult to obtain. To circumvent this difficulty, an additional unknown r_i is defined to condense the contribution of all the cross-coefficient to the flux density $\vec{N}_i$:

$$r_i = \nabla \cdot \left(\sum_{k=1, k \neq i}^{n} L_{ik} \nabla \mu_k \right) \tag{59}$$

The additional variables r_i are determined by minimizing their magnitude subject to a constraint condition. A measure of the magnitude of the inter-ionic fluxes over the domain can be defined as:

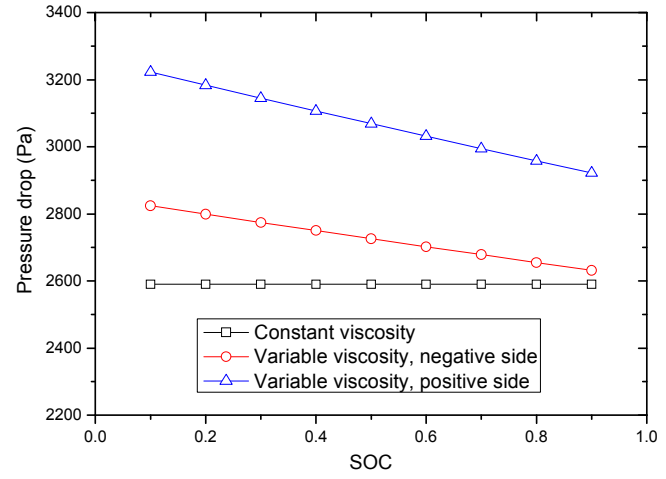

(a)

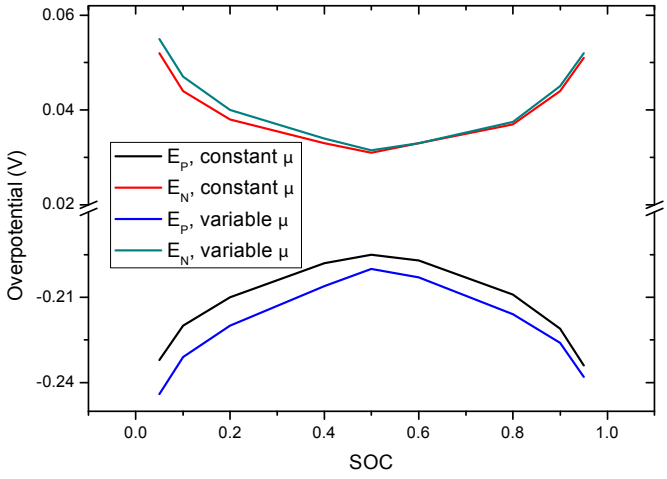

(b)

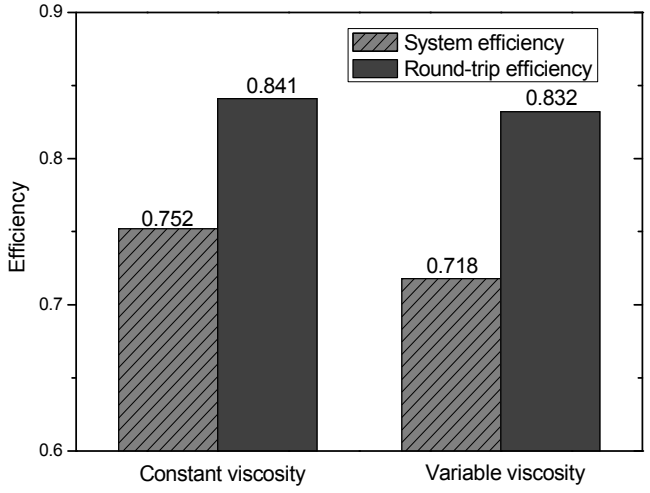

(c)

Fig. 10. Comparisons of the results from the SOC-dependent viscosity model and the constant-viscosity model [108]. (a) Pressure drop; (b) overpotential; and (c) energy-based efficiency and the round-trip efficiency.

$$J(r_1,\ldots,r_n)=\frac{1}{2}\sum_{i=1}^{n}\int_{\Omega} r_i^2 d\Omega \tag{60}$$

The goal is to find the values of the inter-ionic fluxes, r_i, that minimize the above function subjecting to the condition of electroneutrality. This problem can be solved by finding the stationary points of the following function:

$$W(r_1,\ldots,r_n,\lambda)=J(r_1,\ldots,r_n)+\int_{\Omega}\lambda g d\Omega \tag{61}$$

where λ is the Lagrange multiplier and g is the constraint condition of electroneutrality. The stationary points of W represent the smallest magnitudes of r_i that satisfy the electroneutrality.

The equations for the variables are fully coupled. With proper boundary and initial conditions, the unknowns, λ and r_i, can be numerically solved together with the species concentration distributions and cell performance under the condition of non-dilute electrolytes. Comparing the results from the model sans ionic interactions, it is revealed that the contribution of interactions to ionic flow is significant near the ionic sources; this contribution diminishes at areas away from these sources, where the ionic flow can be assumed to be independent [109].

4. Lattice Boltzmann method

The lattice Boltzmann method (LBM) can be viewed as a special discrete form of the Boltzmann Equation, in which the primary variable is the particle velocity distribution function (PDF). The PDF can be updated through the evolution equation, which leads to the computation of the macroscopic density and velocity from the updated PDFs [110].

Recent works have been performed on applying the LBM to the study of transport phenomena in porous media [111–114]. Hao and Cheng [114] simulated the effect of wettability on liquid transport in porous carbon paper using the multiphase free-energy LBM approach. The results show that wettability plays a significant role on water saturation distribution in two-phase flow in the uniform wetting carbon paper. In-plane and through-plane permeability of the anisotropic porous material are simulated for several samples that are reconstructed using the stochastic method by Wiegmann et al. [115,116]. The relationship between the calculated permeability and the porosity is fitted with empirical relations and various fitting constants are determined. Van Doormaal et al. [117] used the LBM to simulate the flow through an idealized porous transport layer, in which the geometry was generated using a Monte Carlo method (MCM). It is shown that the LBM can be used to determine the permeability in a random porous media by solving the flow in the microstructure of the material. It has been further discovered that the fiber arrangement plays a large role in the permeability of the porous layer. Kolyukhin and Espedal [118] simulated the effective permeability of a porous medium and the statistic properties of the flow by double randomization MCM. The results showed that the double randomization gave high accuracy and could improve computational efficiency.

Most recently, Qiu and Sun [110] applied the X-ray computed tomography (XCT) to obtain detailed geometry of the porous electrode of a VRFB (See Fig. 11). The processed XCT data is then used as geometry input for modeling the electrochemical processes in the VRFB. Electrolyte flow through pore spaces (micrometer scale) is modeled using the LBM, while the finite volume method (FVM) is used to solve the coupled species and charge transport and predict the performance of the VRFB under various conditions.

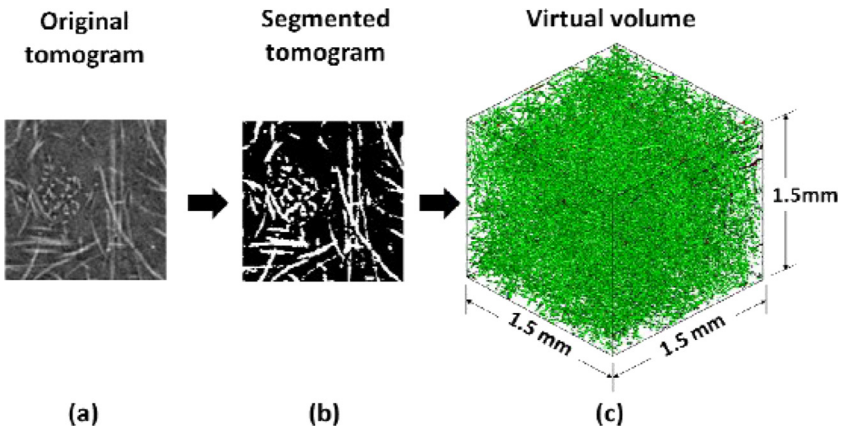

Fig. 11. Procedure for reconstructing microstructural electrode fiber virtual volume using XCT [110]. (a) A tomogram is generated by imaging the electrode material at high resolution; (b) the tomogram is then segmented to distinguish the carbon fibers from the pores; (c) the binary images are stacked together and reconstructed into a virtual volume for further analysis.

This treatment distinguishes between solid electrode and liquid electrolyte phases, thus capturing the effects of electrode geometry on cell performance (See Fig. 12). This novel model provides a useful tool for building the structure-property-performance relationship and is anticipated to be widely applied in flow battery modeling.

5. Molecular dynamics and density function simulations

To understand the underlying chemistry in flow batteries, some molecular/atomic simulations have been performed. The commonly used approaches are Molecular Dynamics (MD) and Density Functional Theory (DFT). Vijayakumar and Yang et al. [119] found that the V^{5+} species exist as $[VO_2(H_2O)_3]^+$ by using MD modeling, which was originally studied experimentally by Skyllas-Kazacos et al. [120,121]. The complex has poor stability at elevated temperatures, leading to the precipitation of V^{5+} in electrolyte solution following the deprotonation of the penta coordinated vanadium ion. At high acid concentrations, such a deprotonation process can be avoided, thus stabilizing the V^{5+} solution. More recently, the same authors investigated the structure of V^{3+} in a mixture of vanadium chloride and vanadium sulfate using NMR spectroscopy and DFT modeling [122]. Based on the study, the counter anions, namely the sulfate and the chloride ions, are expected to play a critical role in the stability of the V^{3+} electrolyte. The results revealed that the precipitation reaction is controlled by the vanadium to proton ratio, in addition to the solution temperature.

Although research on flow batteries is limited so far, the molecular/atomic simulations are important for understanding the molecular/atomic structure and the nature of materials. However, it is worth noting that macroscopic behavior cannot be determined using these approaches. Therefore, a combination of the methods at the molecular/atomic scale and the macro scale may be an option in the model development for flow batteries.

6. Stack-level network models

The models discussed in Section 3 incorporate the fundamental models of transports of mass, momentum, heat and charge, as well as the electrochemical kinetics. It is not feasible, however, to incorporate this level of detail in control/monitoring tools or in modeling flow battery stacks. Therefore, there is a need to develop control-oriented models that can rapidly and accurately capture the performance of flow battery systems. Rather than focusing on the detailed distributions of variables, these models concentrate on the cell performance and system efficiency. Such control-oriented models are called unit- or stack-level network models. Usually, several assumptions are made for the purpose of simplifying the network models [123–125]: the electrolyte is fully filled in the electrolyte tanks; the concentrations in each electrolyte tank, pipe and cell or stack are uniform; the cell or stack and tanks behave as continuous stirred tank reactors; the cell or stack resistance remains constant over the operating range of the flow battery.

Some stack-level network models for different flow batteries are available in the open literature. Shah et al. [124] proposed a so-called unit model for all-vanadium redox flow battery, which takes account of the major components of voltage loss, the electrode kinetics and the recirculation of the half-cell electrolytes. The model is able to relate important characteristics of performance, such as the time to charge/discharge and the SOC, to key system properties. Simulations have demonstrated that the model is able to capture the performance in practical systems to a high degree of accuracy. Recently, Ontiveros and Mercado [126] developed a stack-level network model, which accounts for both the voltage and coulombic losses of the VRFB stack. It does not depend on the parameters that are difficult to obtain from data sheets, and it can be employed for modeling of other electrochemical energy storage systems.

Blanc and Rufer [127] combined the electrochemical model and the mechanical model to develop a multiphysics VRFB system model. With this model, they investigated the optimal operating points at constant current and constant power (See Fig. 13), respectively. Xu and Zhao [128] proposed a power-based efficiency which takes account of both the cell performance and pumping power for the evaluation of flow field designs for VRFBs. Their results indicate that there is an optimal flow rate for each type of flow field at which the maximum power-based efficiency can be achieved. As the cell with the serpentine flow field at the optimal flow rate shows the highest energy-based efficiency and round-trip efficiency (RTE), this type of flow field appears to be more suitable for VRFBs than the parallel flow field does. More recently, Yin and Tang [129] developed a three-dimensional model of VRB with interdigitated flow channel. Their results show that the electrolyte flow rate and stack channel dimension are the critical factors affecting flow distribution and cell performance. The model developed in this paper can be employed to optimize both VRB stack design and system operation conditions design.

In addition, Scamman and Roberts [130] used a utility-scale model to predict the technical and commercial performance of a 120 MWh/15 MW PSB storage plant. Based on the technical and

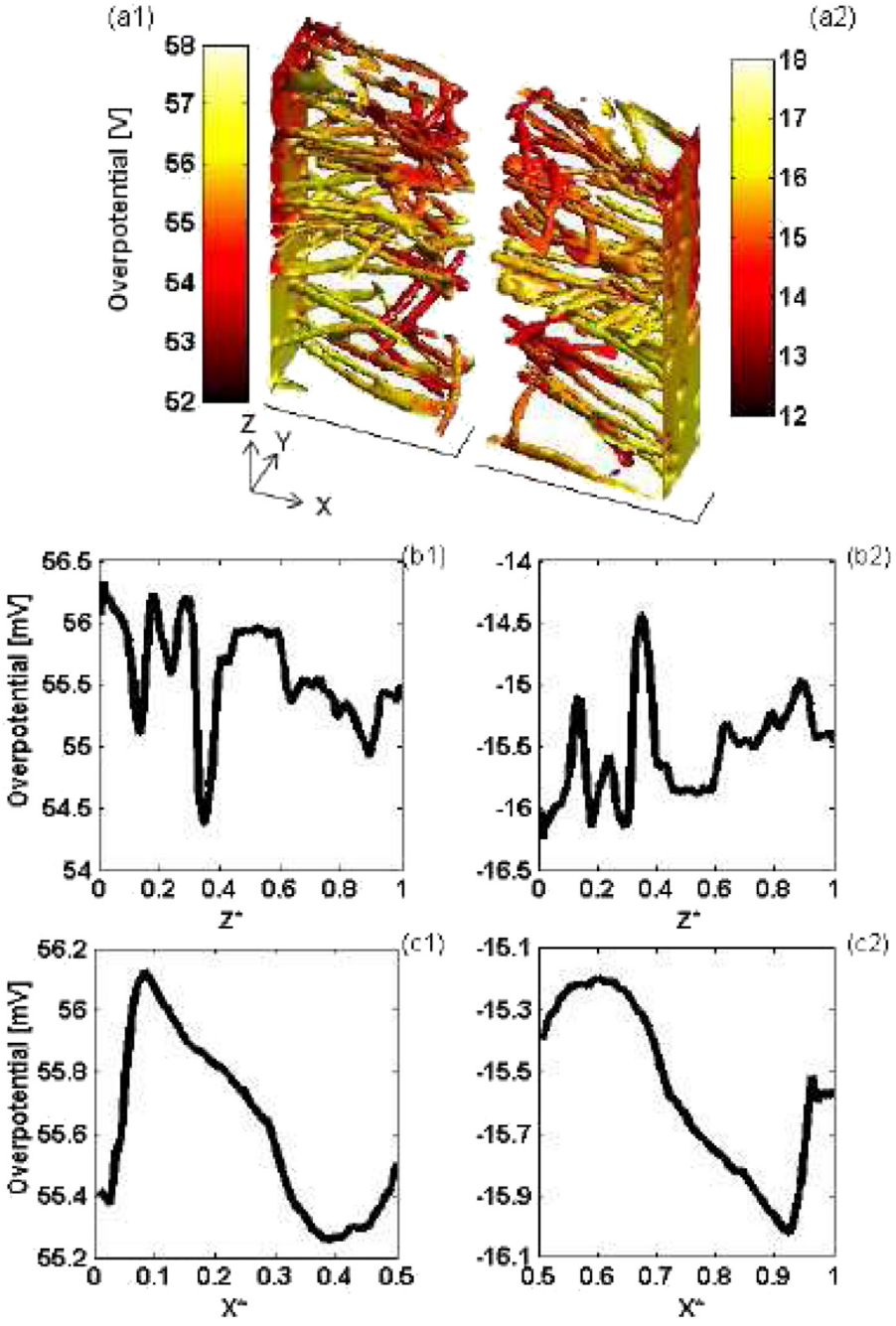

Fig. 12. Pore-scale predictions of overpotential distribution on the active surface with an inlet SOC of 50% during galvanostatic discharge at 400 A/m^2 [110]. Distributions shown are (a) local absolute value on the 3-D surface of the electrode fibers, (b) averaged along electrolyte flow direction, (c) averaged along current flow direction for both the (1) negative and (2) positive half-cell.

commercial parameters used, they claimed a range of current density and electrolyte flow rate to make the plant economic for arbitrage applications.

The shunt current in flow batteries, which refers to a condition in which current deviates from the intended path via a bypass with a sufficiently low resistance to divert a portion of the current, is one of the concerns in stack modeling. Xing and Zhang [131] developed a stack-level model to investigate the shunt current loss of the vanadium redox flow battery. The distribution of shunt current was described and the effect of charge/discharge pattern on shunt current loss was studied. The results show that reducing the number of series-wound single cells, decreasing the resistance of manifolds and channels, and increasing the power of a single cell, are viable further development directions for the VRFB stack.

Codina et al. [132] analyzed the issue of shunt currents in Fe/Cr flow battery when a cell is scaled up to a larger stack. The influences of the length of the hydraulic interconnection in the stack and the assembly current on energy efficiency were also examined. This stack-level model was considered to be used in application, for improving the system efficiency of Fe/Cr flow battery system.

More recently, Tang and Skyllas-Kazacos [125] performed a network model to demonstrate the temperature variation of a VRFB stack. Considering a stack containing 19 cells and two cylindrical electrolyte tanks, the energy balance equations for the battery stack

and the two electrolyte tanks can be respectively described as follows:

$$\frac{\partial}{\partial t}(\rho V_s C_p T_s) = Q_+ C_p \rho (T_+ - T_s) + Q_- C_p \rho (T_- - T_s) + I^2 R \quad (62)$$

$$\frac{\partial}{\partial t}(\rho V_+ C_p T_+) = Q_+ C_p \rho (T_s - T_+) + U_+ A_+ (T_{air} - T_+) \quad (63)$$

$$\frac{\partial}{\partial t}(\rho V_- C_p T_-) = Q_- C_p \rho (T_s - T_-) + U_- A_- (T_{air} - T_-) \quad (64)$$

where T_s is stack electrolyte temperature, T_+ is temperature of the positive electrolyte in the tank, T_- is temperature of the negative electrolyte in the tank, T_{air} is surrounding air temperature, V_s is volume of the battery stack, V_+ is volume of the positive electrolyte in the tank, V_- is volume of the negative electrolyte in the tank, Q_b

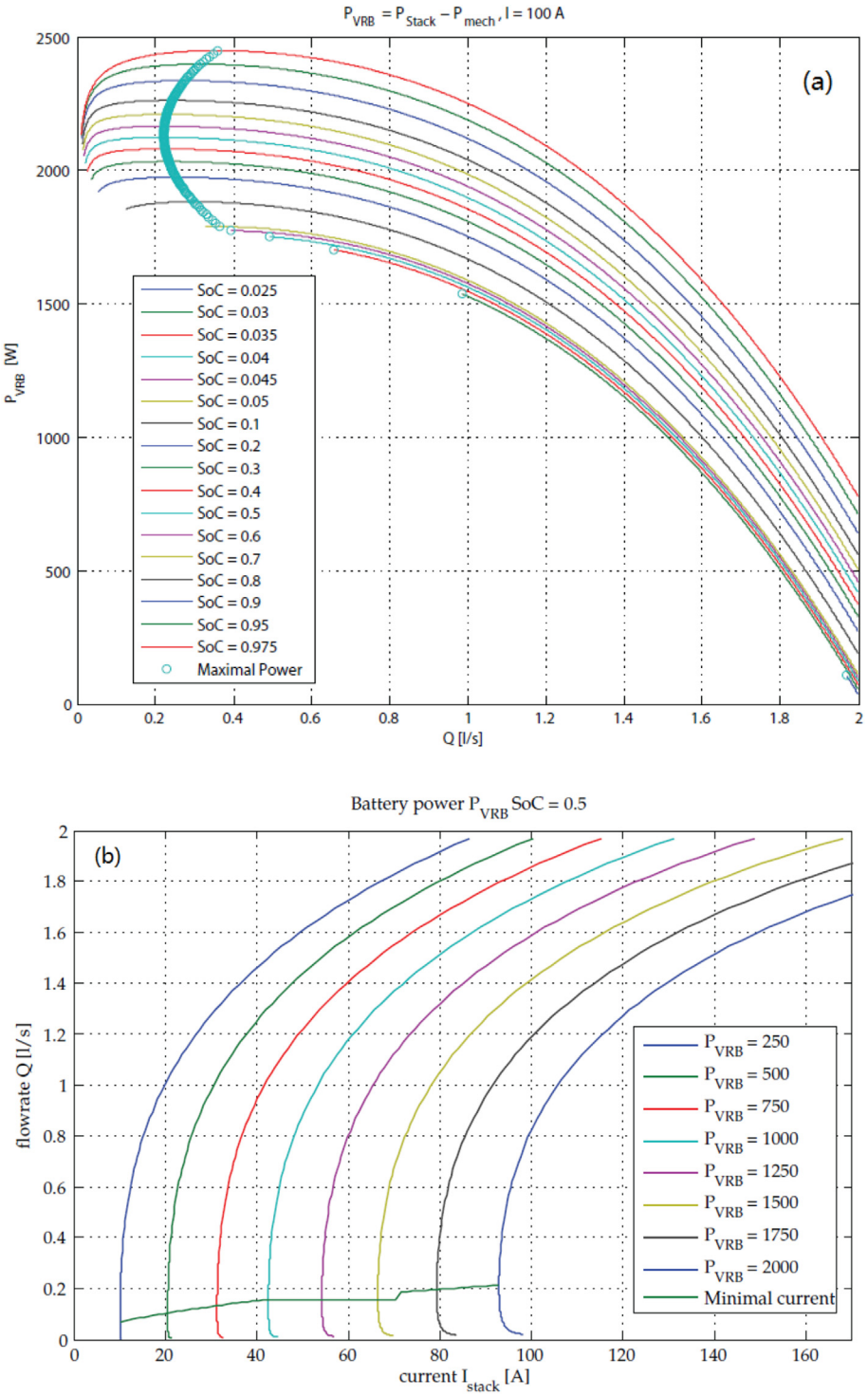

Fig. 13. (a) Optimal flow rate Q_{opt} as a function of the flow rate Q and the SOC during discharge at 100 A. (b) Battery power P_{VRB} as a function of the discharge current I_{stack} and the electrolyte flow rate Q at a SOC of 0.5. The optimal operating points occurs when the current I_{stack} is minimal for a given battery power P_{VRB} [124].

is outlet flow rate of the battery stack, Q_+ is outlet flow rate of the positive electrolyte in the tank, Q_- is outlet flow rate of the negative electrolyte in the tank, U_+ is overall heat transfer coefficient of the tank at positive side, U_- is overall heat transfer coefficient of the tank at negative side, A_+ is surface area of the tank at positive side, A_- is surface area of the tank at negative side and I is the charge or discharge current. The modeling results show that the electrolyte temperatures in both the tanks and stack are influenced by multiple effects of charge/discharge current, flow rate, surrounding temperature and the heat generated by cell resistance (See Fig. 14). Increasing current or reducing flow rate will increase the electrolyte temperature in tanks and stack. Thermal properties of the tank material and its surface area can, however, be adjusted to optimize heat transfer flux to the surroundings to reduce overheating.

7. Summary and outlook

Flow batteries hold an excellent combination of energy efficiency, capital cost and cycle life. Thus, they have attracted widespread research endeavors for several decades, including the development of technology for modeling. In this paper, we review the governing equations for various transport processes such as mass, momentum, heat and charge as well as the electrochemical reactions, and summarize the determinations of key transport properties for porous-medium models in detail. Lattice Boltzmann method, molecular dynamics and density function simulations as well as stack-level network models are also discussed. To remove the commonly used simplifications and develop more advanced modeling technology, there should be particular focus on the following areas:

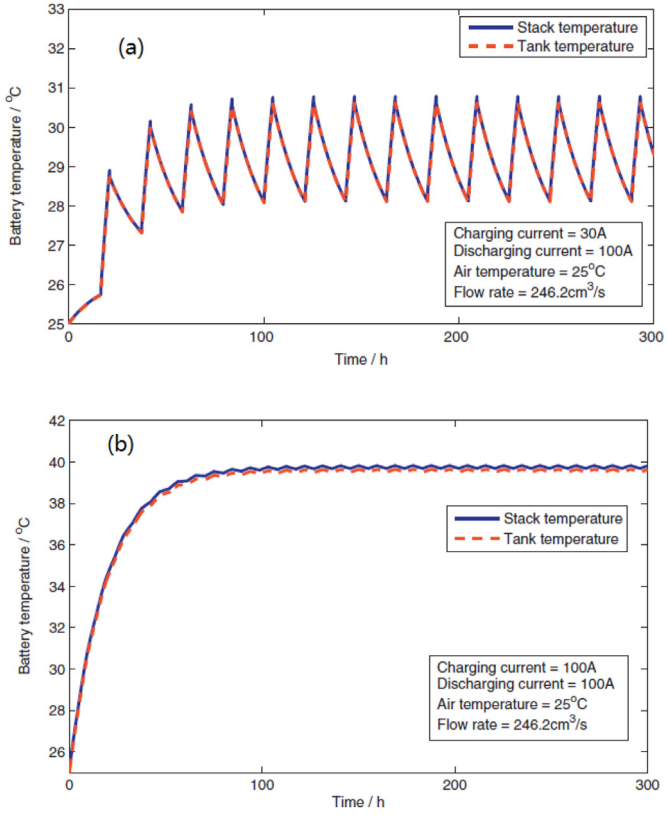

Fig. 14. Battery temperature variations at: (a) 30 A charge current and 100 A discharge current at a constant air temperature of 25 °C; (b) 100 A charge current and 100 A discharge current at a constant air temperature of 25 °C [130].

(1) A better understanding of the redox reaction kinetics on the surface of porous electrodes. Rather than settling with simplified "overall" reactions, detailed descriptions for every reaction step should be determined.
(2) Parameter sensitivity analysis. There are many parameters which affect the performance of flow batteries. Sensitivity analyses can identify the parameters which affect battery performance most significantly.
(3) The mass and heat transfer in the flow battery stack of practical size. As the flow arrangement and heat management are crucially important in the flow battery stack, the modeling results can be used for the optimization of stack structure (e.g. the selection of flow fields, the connection pattern of single cells) and for the control of stack temperature in a rational range.
(4) Multi-scale modeling, in which micro- and macro-scale physicochemical processes could be solved simultaneously.

With the development of modeling technology, the fundamental understanding of the transport and electrochemical processes in flow batteries can be fully unlocked. With the combination of experimental diagnostics, results from modeling can be further used to optimize the specific design, as well as to fine-tune the operating conditions for improved cell performance and ultimately, a reduction in cost. These research directions can help to significantly accelerate the world-wide deployment of flow battery technologies.

Acknowledgments

The work described in this paper was fully supported by a grant from the Research Grants Council of the Hong Kong Special Administrative Region, China (Project No. 623313). One of the authors (Q. Xu) also thanks the support by a grant from the National Natural Science Foundation of China (Grant No. 51306076).

Nomenclature

A_V	specific surface area of the porous electrode ($m^2\ m^{-3}$)
c	concentration ($mol\ m^{-3}$)
D	diffusivity ($m^2\ s^{-1}$)
D_F	mean fiber diameter (m)
E^0	equilibrium potential (V)
F	Faraday constant ($C\ mol^{-1}$)
G	Gibbs free energy ($J\ mol^{-1}$)
I	current density ($A\ m^{-2}$)
$\vec{i}_m$	current density in the solid matrix ($A\ m^{-2}$)
$\vec{i}_s$	current density in the electrolyte solution ($A\ m^{-2}$)
K	permeability of porous material (m^2)
K_{CK}	Carman–Kozeny constant
k	standard reaction rate constant ($m\ s^{-1}$)
k_m	local mass transfer coefficient ($m\ s^{-1}$)
l_{mem}	membrane thickness (m)
$\vec{N}$	molar flux ($mol\ m^{-2}\ s^{-1}$)
P	power (W)
p	pressure (Pa)
Q	volumetric flow rate ($ml\ s^{-1}$)
R	gas constant, 8.314 ($J\ mol^{-1}\ K^{-1}$)
$\dot{R}$	source term in species conservation equation ($mol\ m^{-3}\ s^{-1}$)
S	surface area of the electrode
T	temperature (K)
W	work (J)
$\vec{u}$	superficial velocity ($m\ s^{-1}$)

x	molar fraction
z	stoichiometric coefficient

Greek

α_+	anodic transfer coefficients
α_-	cathodic transfer coefficients
β	system-specific constant for non-ideal solution
ε	porosity of porous electrode
ψ	efficiency
η	overpotential (V)
μ	ionic mobility ($m^2\ V^{-1}\ s^{-1}$)
ν	kinematic viscosity ($m^2\ s^{-1}$)
ρ	density ($kg\ m^{-3}$)
σ	conductivity ($S\ m^{-1}$)
ϕ	potential (V)

Superscripts

0	initial value
eff	effective value
s	value at the pore surface of porous electrode

Subscripts

1	negative electrode
2	positive electrode
char	charge
disch	discharge
H^+	proton
in	inlet
m	solid matrix
mem	membrane
out	outlet
s	solution

References

[1] National Research Council. In: The National Academies Summit on America's Energy Future: summary of a meeting. Washington DC: National Academies Press; 2008.
[2] Skyllas-Kazacos M, Chakrabarti MH, Hajimolana SA, Mjalli FS, Saleem M. Progress in flow battery research and development. J Electrochem Soc 2011;158:R55–79.
[3] Yang ZG, Zhang JL, Liu J. Electrochemical energy storage for green grid. Chem Rev 2011;111:3577–613.
[4] Barton JP, Infield DG. Energy storage and its use with intermittent renewable energy. IEEE Trans Energy Convers 2004;19:441–8.
[5] Electropaedia. Energy sources and energy storage, battery and energy encyclopaedia and history of technology, http://www.mpoweruk.com/performance.html.
[6] Electrical Storage Association. http://www.electricitystorage.org/ESA/tech.html.
[7] Chen H, Cong TN, Yang W, Tan C, Ding Y. A review of the problems of energy storage. Prog Nat Sci 2009;19:291–312.
[8] Soloveichik GL. Battery technologies for large-scale stationary energy storage. Annu Rev Chem Biomol Eng 2011;2:503–27.
[9] Shigematsu T. Redox flow battery for energy storage. SEI Tech Rev 2011;73:4–11.
[10] de Leon CP, Frias-Ferrer A, Gonzalez J, Szanto DA, Walsh FC. Redox flow cells for energy conversion. J Power Sources 2006;160:716–32.
[11] Nguyen T, Savinell RF. Flow batteries. ECS Interface 2010;19:54–6.
[12] Zhang HM. Redox flow battery for energy storage. ECS Trans 2010;28:1–5.
[13] Skyllas-Kazacos M, Kazacos G, Poon G, Verseema H. Recent advances with UNSW vanadium-based redox flow batteries. Int J Energy Res 2010;34:182–9.
[14] Kear G, Shah AA, Walsh FC. Development of the all-vanadium redox flow battery for energy storage: a review of technological, financial and policy aspects. Int J Energy Res 2012;36:1105–20.
[15] Weber AZ, Mench MM, Meyers JP, Ross N, Gostick JT, Liu QH. Redox flow batteries: a review. J Appl Electrochem 2011;41:1137–64.
[16] Yang ZG, Liu J, Baskaran S, Imhoff CH, Holladay JD. Enabling renewable energy and the future grid with advanced electricity storage. JOM 2010;62:14–23.
[17] Dunn B, Kamath H, Tarascon JM. Electrical energy storage for the grid: a battery of choices. Science 2011;334:928–35.
[18] Yue L, Li WS, Sun FQ, Zhao LZ, Xing LD. Highly hydroxylated carbon fibres as electrode materials of all-vanadium redox flow battery. Carbon 2010;48:3079–90.
[19] Han PX, Wang HB, Liu ZH, Chen X, Ma W, Yao JH. Graphene oxide nanoplatelets as excellent electrochemical active materials for VO^{2+}/VO_2^+ and V^{2+}/V^{3+} redox couples for a vanadium redox flow battery. Carbon 2011;49:693–700.
[20] Zhou HT, Zhang HM, Zhao P, Yi BL. A comparative study of carbon felt and activated carbon based electrodes for sodium polysulfide/bromine redox flow battery. Electrochim Acta 2006;51:6304–12.
[21] Hagg CM, Skyllas-Kazacos M. Novel bipolar electrodes for battery applications. J Appl Electrochem 2002;32:1063–9.
[22] Jia CK, Liu JG, Yan CW. A significantly improved membrane for vanadium redox flow battery. J Power Sources 2010;195:4380–3.
[23] Kim SW, Yan JL, Schwenzer B, Yang ZG. Cycling performance and efficiency of sulfonated poly(sulfone) membranes in vanadium redox flow batteries. Electrochem Commun 2010;12:1650–3.
[24] Xing DB, Zhang SH, Yin CX, Jian XG. Effect of amination agent on the properties of quaternized poly(phthalazinone ether sulfone) anion exchange membrane for vanadium redox flow battery application. J Membr Sci 2010;354:68–73.
[25] Qiu JY, Zhang JZ, Zhai ML. Amphoteric ion exchange membrane synthesized by radiation-induced graft copolymerization of styrene and dimethylaminoethyl methacrylate into PVDF film for vanadium redox flow battery applications. J Membr Sci 2009;334:9–15.
[26] Chen DY, Wang SJ, Xiao M, Han DM, Meng YZ. Sulfonated poly (fluorenyl ether ketone) membrane with embedded silica rich layer and enhanced proton selectivity for vanadium redox flow battery. J Power Sources 2010;195:7701–8.
[27] Jossen A, Sauer DU. Advances in redox flow batteries. In: The first international renewable energy storage conference, Gelsenkirchen, Germany; 2006.
[28] Lide DR. CRC handbook of chemistry and physics. Bora Raton, Florida: CRC Press; 2007.
[29] Sum E, Skyllas-Kazacos M. A study of the V(II)/V(III) redox couple for redox flow cell applications. J Power Sources 1985;15:179–90.
[30] Sum E, Rychcik M, Skyllas-Kazacos M. Investigation of the V(V)/V(IV) system for use in the positive half-cell of a redox battery. J Power Sources 1985;16:85–95.
[31] Skyllas-Kazacos M, Robins R. All-valdium redox battery. U.S. Patent 4786567. 1988.
[32] Skyllas-Kazacos M, Peng C, Cheng M. Evaluation of precipitation inhibitors for supersaturated vanadyl electrolytes for the vanadium redox battery. Electrochem Solid State Lett 1999;2:121–2.
[33] Kazacos M, Skyllas-Kazacos M. Evaluation of carbon plastic electrodes in vanadium redox flow battery. J Electrochem Soc 1989;136:2759–60.
[34] Skyllas-Kazacos M. Methods of preparation of redox cells and batteries containing stabilized electrolyte solutions. U.S. Patent 6143443. 2000.
[35] Skyllas-Kazacos M, Cheng M. Vanadium redox cell electrolyte optimization studies. J Appl Electrochem 1990;20:463–7.
[36] Remick RJ, Ang PG. Electrically rechargeable anionically active reduction-oxidation electrical storage-supply system. U.S. Patent 4485154. 1984.
[37] Price A, Bartley S, Male S, Cooley G. A novel approach to utility scale energy storage. Power Eng J 1999;13:122–9.
[38] Morrissey P. A new energy storage technology. Int J Ambient Energy 2000;21:213–20.
[39] Zito R. Process for energy storage and/or power delivery with means for restoring energy. U.S. Patent 5612148. 1997.
[40] Ge S, Yi BL, Zhang HM. Study of a high power density sodium polysulfide/bromine energy storage cell. J Appl Electrochem 2004;34:181–5.
[41] Clarke R, Dougherty B, Mohanta S, Harrison S. In: Abstract 520, Joint International Meeting 206th Meeting of the Electrochemical Society/2004 Fall Meeting of the Electrochemical Society of Japan, Honolulu, Hawaii; October 3–8, 2004.
[42] Leung PK, de-Leon CP, Low C, Shah AA, Walsh FC. Characterization of a zinc–cerium flow battery. J Power Sources 2011;196:5174–85.
[43] Clarke RL, Dougherty BJ, Harrison S, Millington JP. Lanthanide batteries. U.S. Patent Application, International publication number:WO 2004/095602 A2. 2004.
[44] Wills RG, Collins J, Stratton-Campbell D, Low CT, Pletcher D, Walsh FC. Developments in the soluble lead-acid flow battery. J Appl Electrochem 2010;40:955–65.
[45] Pletcher D, Wills R. A novel flow battery: a lead acid battery based on an electrolyte with soluble lead(II) Part II: flow cell studies. Phys Chem Chem Phys 2004;6:1779–85.
[46] Hazza A, Pletcher D, Wills R. A novel flow battery—A lead acid battery based on an electrolyte with soluble lead(II): IV. The influence of additives. J Power Sources 2005;149:103–11.
[47] Pletcher D, Wills R. A novel flow battery-A lead acid battery based on an electrolyte with soluble lead(II): III. The influence of conditions on battery performance. J Power Sources 2005;149:96–102.
[48] Hazza A, Pletcher D. A novel flow battery: a lead acid battery based on an electrolyte with soluble lead(II): I. Preliminary studies. Phys Chem Chem Phys 2004;6:1773–8.
[49] Swette L, Jalan V. NASA CR-174724, DOE/NASA/0262–271. 1984.
[50] Wu H, Selman JR, Hollandsworth RP. Mass transfer and current distribution in a zinc/redox-battery flow cell. Indian J Tech 1986;24:372–80.

[51] Dullien FAL. Porous media: fluid transport and pore structure. 2nd ed. New York: Academic Press Inc.; 1992.
[52] Fetlawi HA, Shah AA, Walsh FC. Modelling the effects of oxygen evolution in the all-vanadium redox flow battery. Electrochim Acta 2010;55:3192–205.
[53] Shah AA, Fetlawi HA, Walsh FC. Dynamic modelling of hydrogen evolution effects in the all-vanadium redox flow battery. Electrochim Acta 2010;55:1125–39.
[54] Wakao N, Iida Y, Tanisho SJ. A note on chromatographic parameter estimation. Chem Eng Jpn 1974;7:438–42.
[55] Amiri A, Vafai K. Transient analysis of incompressible flow through a packed bed. Int J Heat Mass Trans 1998;41:4259–79.
[56] Fetlawi HA, Shah AA, Walsh FC. Non-isothermal modelling of the all-vanadium redox flow battery. Electrochim Acta 2009;55:78–89.
[57] Bayanov IM, Vanhaelst R. The numerical simulation of vanadium redox flow batteries. J Math Chem 2011;49:2013–31.
[58] Li MH, Hikihara T. A coupled dynamical model of redox flow battery based on chemical reaction, fluid flow, and electrical circuit. IEICE Trans Fundam 2008;91:1741–7.
[59] Schmal D, Van-Erkel J, Van-Dnin PJ. Mass transfer at carbon fiber electrodes. J Appl Electrochem 1986;16:422–30.
[60] Shah AA, Li X, Wills RG, Walsh FC. A mathematical model for the soluble lead-acid flow battery. J Electrochem Soc 2010;157:A589–99.
[61] Scamman DP, Reade GW, Roberts EPL. Numerical modelling of a bromide–polysulphide redox flow battery. Part 1: modeling approach and validation for a pilot-scale system. J Power Sources 2009;189:1220–30.
[62] Fedkiw PS, Watts RW. A mathematical model for the Iron/Chromium redox battery. J Electrochem Soc 1984;131:701–9.
[63] Miller DG. Application of irreversible thermodynamics to electrolyte solutions. I. Determination of ionic transport coefficients l_{ij} for isothermal vector transport processes in binary electrolyte systems. J Phys Chem 1966;70:2639–59.
[64] Buck RP. Kinetics of bulk and interfacial ionic motion: microscopic bases and limits for the Nernst-Planck equation applied to membrane systems. J Membr Sci 1984;17:1–62. http://www.sciencedirect.com/science/article/pii/S0376738800813861-item1.
[65] Gattrell M, Park J, MacDougall B, Apte J, McCarthy S, Wu CW. Study of the mechanism of the vanadium 4+/5+ redox reaction in acidic solutions. J Electrochem Soc 2004;151:A123–30.
[66] Meng H, Wang CY. Electron transport in PEFCs. J Electrochem Soc 2004;151:A358–67.
[67] Teng XG, Zhao YT, Xi JY, Wu ZH, Qiu XP, Chen LQ. Nafion/organically modified silicate hybrids membrane for vanadium redox flow battery. J Power Sources 2009;189:1240–6.
[68] Weber AZ, Newman J. Modeling transport in polymer-electrolyte fuel cells. Chem Rev 2004;104:4679–726.
[69] Bucciantini L, Farina A, Fasano A. Flows in porous media with erosion of the solid matrix. Netw Heterog Media 2010;5:63–95.
[70] Ingmanson WL, Andrews BD, Hohnson RC. Internal pressure distributions in compressible mats under fluid stress. Tappi 1959;42:840–9.
[71] Boomsma K, Poulikakos D. The effects of compression and pore size variations on the liquid flow characteristics in metal foams. ASME J Fluids Eng 2002;124:263–72.
[72] Tadrist L, Miscevic M, Rahli O, Topin F. About the use of fibrous materials in compact heat exchangers. Exp Therm Fluid Sci 2004;28:193–9.
[73] Young JB, Todd B. Modeling of multi-component gas flows in capillaries and porous solids. Int J Heat Mass Trans 2005;48:5338–53.
[74] Tang GH, Tao WQ, He YL. Thermal boundary condition for the thermal lattice Boltzmann equation. Phys Rev E 2005;72:056301–8.
[75] Despois JF, Mortensen A. Permeability of open-pore microcellular materials. Acta Mater 2005;53:1381–8.
[76] Dukhan N. Correlations for the pressure drop for flow through metal foam. Exp Fluids 2006;41:665–72.
[77] Kitanidis PK. Effective hydraulic conductivity for gradually varying flow. Water Resour Res 1990;26:1197–208.
[78] White CD, Horne RN. Computing absolute transmissibility in the presence of fine-scale heterogeneity. In: SPE Symposium on Reservoir Simulation, San Antonio, USA; 1987.
[79] Durlofsky LJ. Numerical calculation of equivalent grid block permeability tensors for heterogeneous porous media. Water Resour Res 1991;27:699–708.
[80] Torquato S. Relationship between permeability and diffusion-controlled trapping constant of porous media. Phys Rev Lett 1990;64:2644–9.
[81] Avellaneda M, Torquato S. Rigorous link between fluid permeability, electrical eonductivity, and relaxation times for transport in porous media. Phys Fluids A 1991;3:2529–40.
[82] Kostek S, Schwartz LM, Johnson DJ. Fluid permeability in porous media: comparison of electrical estimates with hydrodynamical calculations. Phys Rev B 1992;45:186–95.
[83] Martys N, Garboczi E. Length scales relating the fluid permeability and electrical conductivity in random two-dimensional model porous media. Phys Rev B 1992;46:6080–90.
[84] Straley C, Matteson A, Feng S. Magnetic resonance, digital image analysis, and permeability of porous media. Appl Phys Lett 1987;51:1146–9.
[85] Schwartz LM, Martys N, Torquato S. Cross-property relations and permeability estimation in model porous media. Phys Rev E 1993;48:4584–91.
[86] Verbrugge M. Ion and solvent transport in ion-exchange membranes. J Electrochem Soc 1990;137:886–93.
[87] Shah AA, Watt MJ, Walsh FC. A dynamic performance model for redox-flow batteries involving soluble species. Electrochim Acta 2008;53:8087–100.
[88] You DJ, Zhang HM, Chen J. A simple model for the vanadium redox battery. Electrochim Acta 2009;54:6827–36.
[89] Vynnycky M. Analysis of a model for the operation of a vanadium redox battery. Energy 2011;36:2242–56.
[90] Luo XL, Lu ZZ, Chen LQ, Qiu XP. Influences of permeation of vanadium ions through PVDF-g-PSSA membranes on performances of vanadium redox flow batteries. J Phys Chem B 2005;109:20310–4.
[91] Qiu JY, Li MY, Zhai ML, Wei GS. Preparation of ETFE-based anion exchange membrane to reduce permeability of vanadium ions in vanadium redox battery. J Membr Sci 2007;297:174–80.
[92] Jia CK, Liu JG, Yan CW. A multilayered membrane for vanadium redox flow battery. J Power Sources 2012;203:190–4.
[93] Pant LM. MPhil Thesis. University of Alberta; 2011.
[94] Xu Q, Zhao TS. Determination of the mass-transport properties of vanadium ions through the porous electrodes of vanadium redox flow batteries. Phys Chem Chem Phys 2013;15:10841–8.
[95] Xu Q. Ph.D Thesis. The Hong Kong University of Science and Technology; 2013.
[96] Mohammadi T, Chieng SC, Skyllas-Kazacos M. Water transport study across commercial ion exchange membranes in the vanadium redox flow battery. J Membr Sci 1997;133:151–9.
[97] Wiedemann E, Heintz A, Lichtenthaler RN. Sorption isotherms of vanadium with H_3O^+ ions in cation exchange membranes. J Membr Sci 1998;141:207–13.
[98] Sukkar T, Skyllas-Kazacos M. Water transfer behaviour across cation exchange membranes in the vanadium redox battery. J Membr Sci 2003;222:235–47.
[99] Sun CX, Chen J, Zhang HM. Investigations on transfer of water and vanadium ions across Nafion membrane in an operating vanadium redox flow battery. J Power Sources 2010;195:890–7.
[100] Tang A, Bao J, Skyllas-Kazacos M. Dynamic modelling of the effects of ion diffusion and side reactions on the capacity loss for vanadium redox flow battery. J Power Sources 2011;196:10737–47.
[101] Skyllas-Kazacos M, Goh L. Modeling of vanadium ion diffusion across the ion exchange membrane in the vanadium redox battery. J Membr Sci 2012;399:43–8.
[102] Tang A, Bao J, Skyllas-Kazacos M. Thermal hydraulic behavior and efficiency analysis of an all-vanadium redox flow battery. J Power Sources 2013;242:314–24.
[103] Knehr KW, Agar E, Dennison C, Kalidindi A, Kumbur EC. A transient vanadium flow battery model incorporating vanadium crossover and water transport through the membrane. J Electrochem Soc 2012;159:A1446–59.
[104] Knehr KW, Kumbur EC. Role of convection and related effects on species crossover and capacity loss in vanadium redox flow batteries. Electrochem Commun 2012;23:76–9.
[105] Blanc C. Ph.D thesis. EPF Lausanne, Switzerland: 2009.
[106] Hu YF, Lee H. Prediction of viscosity of mixed electrolyte solutions based on the Eyring's absolute rate theory and the semi-ideal hydration model. Electrochim Acta 2003;48:1789–96.
[107] Hu YF. Prediction of viscosity of mixed electrolyte solutions based on the Eyring's absolute rate theory and the equations of Patwardhan and Kumar. Chem Eng Sci 2004;59:2457–64.
[108] Xu Q, Zhao TS. Effects of SOC-dependent electrolyte viscosity on performance of vanadium redox flow batteries. Appl Energy 2014;130:139–47.
[109] Sarkar S, Aquino W. Electroneutrality and ionic interactions in the modeling of mass transport in dilute electrochemical systems. Electrochim Acta 2011;56:8969–78.
[110] Qiu G, Joshi AS, Kumbur EC, Sun Y. 3-D pore-scale resolved model for coupled species/charge/fluid transport in a vanadium redox flow battery. Electrochim Acta 2012;64:46.
[111] Wang LP, Afsharpoya B. Modeling fluid flow in fuel cells using the lattice-Boltzmann approach. Math Comput Simulat 2006;72:242–8.
[112] Joshi AS, Grew KN, Peracchio AA, Chiu WS. Lattice Boltzmann modeling of 2D gas transport in a solid oxide fuel cell anode. J Power Sources 2007;164:631–8.
[113] Park J, Matsubara M, Li X. Application of lattice Boltzmann method to a micro-scale flow simulation in the porous electrode of a PEM fuel cell. J Power Sources 2007;173:404–14.
[114] Hao L, Cheng P. Lattice Boltzmann simulations of anisotropic permeabilities in carbon paper gas diffusion layers. J Power Sources 2009;186:104–14.
[115] Schulz VP, Becker J, Wiegmann A, Mukherjee PP, Wang CY. Modeling of two-phase behaviour in the gas diffusion medium of PEFCs via full morphology approach-Fuel cells and energy conversion. J Electrochem Soc 2007;154:B419–26.
[116] Schladitz K, Peters S, Reinel D, Wiegmann A, Ohser J. Design of acoustic trim based on geometric modeling and flow simulation for non-woven. Comput Mater Sci 2006;38:56–66.
[117] Van-Doormaal MA, Pharoah JG. Determination of permeability in fibrous porous media using the lattice Boltzmann method with application to PEM fuel cells. Int J Numer Meth Fluids 2009;59:75–89.

[118] Kolyukhin D, Espedal M. Numerical calculation of effective permeability by double randomization Monte Carlo method. Int J Numer Anal Model 2010;7:607–18.
[119] Vijayakumar M, Li L, Graff G, Liu J, Zhang H, Yang Z. Towards understanding the poor thermal stability of V^{5+} electrolyte solution in vanadium redox flow batteries. J Power Sources 2011;196:3669–72.
[120] Kausar N, Howe R, Skyllas-Kazacos M. Raman spectroscopy studies of concentrated Vanadium (V) positive redox cell electrolytes. J Appl Electrochem 2001;31:1327–32.
[121] Skyllas-Kazacos M, Menictas C, Kazacos M. Thermal stability of concentrated V(V) electrolytes in the Vanadium redox cell. J Electrochem Soc 1996;143:L86–8.
[122] Vijayakumar M, Li L, Nie Z, Yang Z, Hu J. Structure and stability of hexa-aqua V(III) cations in vanadium redox flow battery electrolytes. Phys Chem Chem Phys 2012;14:10233–42.
[123] Tang A, Bao J, Skyllas-Kazacos M. Thermal modelling of battery configuration and self-discharge reactions in vanadium redox flow battery. J Power Sources 2012;216:489–501.
[124] Shah AA, Tangirala R, Walsh FC. A dynamic unit cell model for the all-vanadium flow battery batteries and energy storage. J Electrochem Soc 2011;158:A671–7.
[125] Tang A, Ting S, Bao J, Skyllas-Kazacos M. Thermal modelling and simulation of the all-vanadium redox flow battery. J Power Sources 2012;203:165–76.
[126] Ontiveros LJ, Mercado PE. Modeling of a vanadium redox flow battery for power system dynamic studies. Int J Hydrogen Energy 2014;39:8720–7.
[127] Blanc C, Rufer A. Understanding the vanadium redox flow batteries. InTech Press; 2010.
[128] Xu Q, Zhao TS, Leung PK. Numerical investigations of flow field designs for vanadium redox flow batteries. Appl Energy 2013;105:47–56.
[129] Yin C, Gao Y, Guo S, Tang H. A coupled three dimensional model of vanadium redox flow battery for flow field designs. Energy 2014;74:886–95.
[130] Scamman DP, Reade GW, Roberts EP. Numerical modelling of a bromide-polysulphide redox flow battery. Part 2: evaluation of a utility-scale system. J Power Sources 2009;189:1231–9.
[131] Xing F, Zhang HM, Ma XK. Shunt current loss of the vanadium redox flow battery. J Power Sources 2011;196:10753–7.
[132] Codina G, Aldaz A. Scale-up studies of an Fe/Cr redox flow battery based on shunt current analysis. J Appl Electrochem 1992;22:668–74.